

INTERNATIONAL SCIENTIFIC JOURNAL

**MATHEMATICAL
MODELING**

YEAR III, — ISSUE 4/2019
ISSN (PRINT) 2535-0986
ISSN (WEB) 2603-2929

Published by
SCIENTIFIC-TECHNICAL UNION of MECHANICAL ENGINEERING - INDUSTRY 4.0
Sofia, BULGARIA

INTERNATIONAL EDITORIAL BOARD

EDITOR I CHIEF

Prof. ANDREY FIRSOV Peter the Great St.Petersburg Polytechnic University	RU
---	----

Members:		
Abilmazhin Adamov, Prof.	L.N.Gumilyov Eurasian National University	KZ
Alexander Guts, Prof.	Omsk State University	RU
Alexei Zhabko, Prof.	Saint Petersburg State University	RU
Andrey Markov, Prof.	Baltic State Technical University	RU
Andrii Matviichuk, Prof.	Kyiv National Economics University	UA
Andrzej Nowakowski, Prof.	University of Lodz	PL
Anton Makarov, Dr.	Saint Petersburg State University	RU
Armands Gricans, Assoc. Prof.	Daugavpils University	LV
Artūras Dubickas, Prof.	Vilnius University	LT
Avinir Makarov, Prof.	Saint Petersburg State University of Industrial Technologies and Design	RU
Christo Boyadjiev, Prof.	Institute of Chemical Engineering, BAS	BG
Daniela Marinova, Dssoc. Prof.	Technical University of Sofia	BG
Dimitrios Poulakis, Prof.	Aristotle University of Thessaloniki	GR
Evgeniy Smirnov, Assoc. Prof.	Volgograd State Technical University	RU
Galia Angelova, Prof. DSc,	Bulgarian Academy of Science	BG
Giovanni Borgioli, Assoc. Prof.	University of Florence	IT
Haskiz Coskun, Prof.	Karadeniz Technical University of Trabzon	TR
Idilia Bachkova, Prof.	University of Chemical Technology and Metallurgy	BG
Igor Anufriev, Assoc. Prof.	Peter the Great St.Petersburg Polytechnic University	RU
Irena Stojkovska, Prof.	Ss. Cyril and Methodius University in Skopje	MK
Ivana Štajner-Papuga, Prof.	University of Novi Sad	RS
Kanagat Aldazharov, Assoc. Prof.	Kazakh Economics University	KZ
Karl Kunisch, Prof.	University of Graz	AT
Mahomed Agamirza ogly Dunyamalyev, Prof.	Azerbaijan Technical University	AZ
Marius Giuclea, Prof.	The Bucharest University of Economics Studies	RO
Mihail Okrepilov, Prof.	D.I. Mendeleev Institute for Metrology (VNIIM)	RU
Milena Racheva, Assoc. Prof.	Technical University of Gabrovo	BG
Mohamed Kara, Dr.	Ferhat Abbas Sétif 1 University	DZ
Mohamed Taher El-mayah, Prof	MTI University	EG
Neli Dimitrova, Prof.	Institute of Mathematics and Informatics, BAS	BG
Nina Bijedic, Prof.	Dzermal Bijedic University of Mostar	BA
Oleg Obradović, Prof.	University of Montenegro	ME
Olga Pritomanova, Assoc. Prof.	Oles Honchar Dnipropetrovsk National University	UA
Özkan Öcalan, Prof.	Akdeniz University of Antalya	TR
Pașc Găvrută, Prof.	Politehnic University of Timisoara	RO
Pavel Satrapa, Assoc. Prof.	Technical University of Liberec	CZ
Pavel Tvrdík, Prof.	Czech Technical University in Prague	CZ
Pavlina Yordanova, Assoc. Prof.	Shumen University	BG
Petr Trusov, Prof.	Perm State Technical University	RU
Rannveig Björnsdóttir, Prof.	University of Akureyri	IS
Roumen Anguelov, Prof.	University of Pretoria	ZA
Sándor Szabó, Dr. Prof.	University of Pécs	HU
Sashko Martinovski, Assoc. Prof.	St. Kliment Ohridski University of Bitola	MK
Sergey Bosnyakov, Prof.	Moscow Institute of Physics and Technology	RU
Sergey Kshevetskii, Prof.	Immanuel Kant Baltic Federal University	RU
Snejana Hristova, Prof.	University of Plovdiv	BG
Svetlana Lebed, Assoc. Prof.	Brest State Technical University	BY
Tomasz Szarek, Prof.	University of Gdansk	PL
Valeriy Serov, Prof.	University of Oulu	FI
Vasily Maximov, Prof.	Saint Petersburg State University of Industrial Technologies and Design	RU
Ventsi Rumchev, Prof.	Curtin University, Perth	AU
Veronika Stoffová, Prof.	University of Trnava	SK
Veselka Pavlova, Prof.	University of National and World Economy	BG
Viorica Sudacevschi, Assoc. Prof.	Technical University of Moldova	MD
Vladimir Janković, Prof.	University of Belgrade	RS
Vladislav Holodnov, Prof.	Saint Petersburg State Institute of Technology	RU
Vyacheslav Demidov, Prof.	Saint Petersburg State University of Industrial Technologies and Design	RU
Yordan Yordanov, Assoc. Prof.	University of Sofia	BG
Yuriy Kuznetsov, Prof.	Nizhny Novgorod State University	RU
Zdenka Kolar - Begović, Prof.	University of Osijek	HR

INTERNATIONAL SCIENTIFIC JOURNAL

MATHEMATICAL MODELING

PUBLISHER:

SCIENTIFIC TECHNICAL UNION OF MECHANICAL ENGINEERING
“INDUSTRY 4.0”

108, Rakovski Str., 1000 Sofia, Bulgaria

tel. (+359 2) 987 72 90,

tel./fax (+359 2) 986 22 40,

office@stumejournals.com

www.stumejournals.com

ISSN (PRINT) 2535-0986

ISSN (WEB) 2603-2929

YEAR III, ISSUE 4 / 2019

EDITOR IN CHIEF:

Prof. D.Sc. ANDREY FIRSOV

Peter the Great St.Petersburg Polytechnic University, Russia

CONTENTS

THEORETICAL FOUNDATIONS AND SPECIFICITY OF MATHEMATICAL MODELLING

MATHEMATICAL AND NUMERICAL SIMULATION OF STRESSES AND DISPLACEMENTS LOCALIZATION PROBLEMS

PhD. Zirakashvili Natela 101

MODELING OF A CYLINDRICAL BODY MOTION ON A VIBRATING SURFACE

Doctor of Physical and Mathematics sciences, Prof. Ibrayev A.,

Candidate of Physical and Mathematics sciences, Assoc. Prof. Bersugir M. 105

APPLICATION OF PERSISTENT HOMOLOGY ON BIO-MEDICAL DATA – A CASE STUDY

Eng. Sekuloski, P., Ass. Prof. Dr. Dimitrievska Ristovska, V. 109

MATHEMATICAL MODELLING OF TECHNOLOGICAL PROCESSES AND SYSTEMS

MULTIPARAMETER HYBRID NEURAL NETWORK METAMODEL OF EDDY CURRENT PROBES WITH VOLUMETRIC STRUCTURE OF EXCITATION SYSTEM

Trembovetska R., PhD Eng., Assoc. Prof. ; Halchenko V., Dr.Sc. Eng., Prof. ; Tychkov V., PhD Eng.,

Assoc. Prof. 113

MODELING THE NUMBER OF ERRORS THAT THE CODE SURELY DETECTS

Prof. Ilievska N. PhD. 117

MODELING OF OVERLAP AREA OF POWDER FILTER MATERIALS

Prof., Dr. Eng., Cor. Member of NAS of Belarus Ilyushchanka A., Head of the Lab. Charniak I.,

Res. Zhehzdryn D., Dr. Eng., Docent Kusin R. 121

MATHEMATICAL MODELING OF THE OPERATING SYSTEM OF THE CAROUSEL TYPE TRANSPLANTING MACHINE

Ass. Prof., PhD, Iurie Melnic, PhD student Vladimir Melnic 124

RESEARCH OF MATHEMATICAL MODELS OF LITHIUM-ION STORAGEES

PhD (Technical), Associate Professor, Plakhtii O., PhD (Technical), Associate Professor, Nerubatskyi V.,

Postgraduate, Philipjeva M., Postgraduate, Mashura A. 127

MATHEMATICAL AND NUMERICAL SIMULATION OF STRESSES AND DISPLACEMENTS LOCALIZATION PROBLEMS

PhD. Zirakashvili Natela

I. Vekua Institute of Applied Mathematics of Iv. Javakishvili Tbilisi State University, Georgia

natzira@yahoo.com

Abstract: *Mathematical and numerical simulation of the non-classical problems, namely problems of localization of stresses and displacements in the elastic body, are obtained by the boundary element method. The current work examines two localization problems, which have the following physical sense: on the middle point of the segment lying inside a body parallel to the border half plane in first case a point force is applied, and we must find such value of the normal stress along the section of the border half plane, which will cause this point force, while in the second case, there is given a vertical narrow deep trench outgoing of this point, and we must find such value of the normal stress along the section of the border half plane, which will result in such a pit. By using MATLAB software, the numerical results are obtained and corresponding graphs are constructed.*

Keywords: NON-CLASSICAL PROBLEM, BOUNDARY ELEMENT METHOD, LOCALIZATION PROBLEM, HOMOGENEOUS ISOTROPIC HALF PLANE

1. Introduction

In the present work, mathematical and numerical simulation of the problems of localization of stresses and displacements in a body, are gained by the boundary element method (BEM) [1]. In a certain sense, the problem of localization of stresses in the elastic body is the inverse problem to the delocalization problem [2]. The localization problem is defined as follows: to change a sufficiently uniform stressed-deformed state of a body for a sharply expressed non-uniform stressed-deformed state (in conditions of constant external perturbations) by changing and appropriate selection of parameters of the medium.

In the theory of elasticity, there are a number of problems [3]-[10] that could be called non-classical due to the fact that boundary conditions on a part of the boundary surface or on the entire boundary surface are either over-determined or underdetermined, or the conditions on the boundary are connected with the conditions inside the body (so called non-local problems).

The current article sets and solves non-classical two-dimensional elasticity problems by using BEM, and problems of localization of stress and displacement for a homogeneous isotropic elastic half-plane are formulated based on them. The present paper examines two localization problems, which have the following physical meaning: on the middle point of the segment lying inside a body parallel to the border half plane in first case a point force is applied, and we must find such value of the normal stress along the section of the border half plane, which will cause this point force (stresses localization), while in the second case, there is given a vertical narrow deep trench outgoing of this point, and we must find such value of the normal stress along the section of the border half plane, which will result in such a pit (displacements localization).

Finally, there are test examples given showing the value of normal stress supposed to apply to the section of the half-plane boundary to obtain the pre-given localized stress or displacement at the midpoint of the segment inside the body. The numerical results of these problems are obtained and presented appropriate graphs, and mechanical and physical interpretations of the problems.

2. Formulation of problems

Let us set some non-classical static problems for homogeneous isotropic half plane (see. Fig.1).

It is known that a homogeneous system of elastic static equilibrium in displacements in the Cartesian system of coordinates has the form [16]

$$\begin{cases} (\lambda + \mu)\theta_{,x} + \mu\Delta u = 0 \\ (\lambda + \mu)\theta_{,y} + \mu\Delta v = 0 \end{cases} \quad \text{in } D \quad (1)$$

where $\lambda = \frac{\nu E}{(1-2\nu)(1+\nu)}$, $\mu = \frac{E}{2(1+\nu)}$ are Lamé constants, E is elasticity modulus, and ν Poissons's ratio; $\Delta(\cdot) = (\cdot)_{,xx} + (\cdot)_{,yy}$ is a Laplacian, $\theta = \text{div } \vec{U} = u_{,x} + v_{,y}$; $\vec{U} = (u, v)$ is the displacement vector; $(\cdot)_{,x} = \frac{\partial(\cdot)}{\partial x}$, $(\cdot)_{,y} = \frac{\partial(\cdot)}{\partial y}$; $(\cdot)_{,xx} = \frac{\partial^2(\cdot)}{\partial x^2}$; $(\cdot)_{,yy} = \frac{\partial^2(\cdot)}{\partial y^2}$.

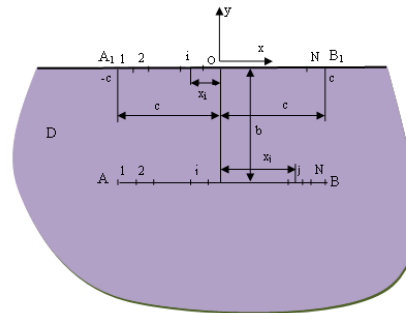


Fig. 1 Illustration of localization problems of stresses and displacements for elastic half plane.

2.1. Statement and solving of problem when normal stress is applied to segment inside half plane

(a) Setting. Let us consider a non-classical problem for half plane D (see Fig. 1), when the tangent stress along the entire border and normal stress along boundary segment $|x| > c, y = 0$ equal to zero. Along segment $|x| \leq c, y = -b$ inside the body, the value of normal stress σ_{yy} is known. So, let us find the solutions to the system of equilibrium equations (1) satisfying the following boundary conditions:

$$\begin{aligned} \text{for } |x| < \infty \text{ and } y = 0: \quad & \sigma_{xx} = 0, \\ \text{for } |x| > c \text{ and } y = 0: \quad & \sigma_{yy} = 0, \\ \text{for } |x| \leq c \text{ and } y = -b: \quad & \sigma_{yy} = -P_0(x), \end{aligned}$$

where $P_0(x)$ is the sufficiently smooth function given along segment $[-c; c]$.

We can formulate the set problem as follows: let us find the kind of distribution of normal stress σ_{yy} along section $|x| \leq c, y = 0$ of the boundary of a half plane (see Fig. 1) so that the normal stress along segment $|x| \leq c, y = -b$ inside the body equals to the values of given function $P_0(x)$.

If we consider function of kind $P_0(x) = P \cdot 10^{-|x|}$ ($P = \text{constant}$), which describes a force similar to the concentrated

one, then we will have the following localization problem: we must find the kind of distribution of normal stress σ_{yy} along segment A_1B_1 to obtain the concentrated force of the given value (localization of stresses) along section AB (see Fig. 1).

(b) Solution. Let us divide segments $|x| \leq c, y = 0$ and $|x| \leq c, y = b$ into N segments (elements) of the same size $2a$ and smaller sizes (i.e. $a = c/N$). We mean that constant normal stresses P_y^j act on each j^{th} element of length $2a$ with center $(x^j; 0)$ of segment $|x| \leq c, y = 0$. We need to find such values of these stresses, for which the values of the normal stresses in middle points $(x^i, -b)$ of each i^{th} segment with a length of $2a$ along segment $|x| \leq c, y = -b$ inside body will equal to the given value of $-P_0(x^i)$.

Normal stress in the centre of the i^{th} element lying on segment $|x| \leq c, y = -b$ will equal to following sum:

$$\sigma_{yy}(x^i, -b) = \sum_{j=1}^N A^{\#} P_y^j, \quad i = 1, 2, \dots, N,$$

where for the influence coefficients $A^{\#}$ has the following formula

$$A^{\#} = -\frac{1}{\pi} \left[\left(\arctan \frac{b}{x^i - x^j - a} - \arctan \frac{b}{x^i - x^j + a} \right) + \frac{b(x^i - x^j + a)}{(x^i - x^j + a)^2 + b^2} - \frac{b(x^i - x^j - a)}{(x^i - x^j - a)^2 + b^2} \right].$$

Thus, we obtain the following system of N linear algebraic equations with N unknown quantities $P_y^j, j = 1, 2, \dots, N$.

$$\sum_{j=1}^N A^{\#} P_y^j = P_0(x^i), \quad i = 1, 2, \dots, N. \quad (2)$$

If solving (2) system in relation to unknown quantities P_y^j by means of any standard method of numerical analysis (by method of Gauss in our case), then we can assume that the set problem is solved and $\sigma_{yy}^j = P_y^j, j = 1, \dots, N$.

After solving these equations, we can express the displacements and stresses at any point (x^i, y^k) of the body by means of other linear combination of load P_y^j . For example, the stresses and displacements have the following form:

$$\begin{aligned} \sigma_{xx}(x^i, y^k) &= \frac{1}{\pi} \sum_{j=1}^N \left[\left(\arctan \frac{y^k}{x^i - x^j - a'} - \arctan \frac{y^k}{x^i - x^j - a''} \right) - \frac{y^k(x^i - x^j + a')}{(x^i - x^j + a')^2 + (y^k)^2} + \frac{y^k(x^i - x^j - a'')}{(x^i - x^j - a'')^2 + (y^k)^2} \right] P_y^j, \\ \sigma_{yy}(x^i, y^k) &= \frac{1}{\pi} \sum_{j=1}^N \left[\left(\arctan \frac{y^k}{x^i - x^j - a'} - \arctan \frac{y^k}{x^i - x^j + a''} \right) - \frac{y^k(x^i - x^j + a')}{(x^i - x^j + a')^2 + (y^k)^2} + \frac{y^k(x^i - x^j - a'')}{(x^i - x^j - a'')^2 + (y^k)^2} \right] P_y^j, \\ \sigma_{xy}(x^i, y^k) &= \frac{1}{\pi} \sum_{j=1}^N (y^k)^2 \left[\frac{1}{(x^i - x^j + a')^2 + (y^k)^2} - \frac{1}{(x^i - x^j - a'')^2 + (y^k)^2} \right] P_y^j, \end{aligned} \quad (3)$$

$i = 1, 2, \dots, M_1, \quad k = 1, 2, \dots, M_2.$

$$\begin{aligned} u_x^i(x^i, y^k) &= -\frac{1}{2\pi\mu} \sum_{j=1}^N \left\{ (1-2\nu) \left[(x^i - x^j - a') \arctan \frac{y^k}{x^i - x^j - a'} - (x^i - x^j + a) \arctan \frac{y^k}{x^i - x^j + a'} - \pi a \right] \right. \\ &\quad \left. + (1-\nu) y^k \ln \frac{(x^i - x^j - a')^2 + (y^k)^2}{(x^i - x^j + a')^2 + (y^k)^2} \right\} P_y^j, \end{aligned}$$

$$\begin{aligned} u_y^i(x^i, y^k) &= \frac{1}{2\pi\mu} \sum_{j=1}^N \left\{ -y^k (1-2\nu) \left(\arctan \frac{y^k}{x^i - x^j - a'} - \arctan \frac{y^k}{x^i - x^j + a'} \right) \right. \\ &\quad \left. + (1-\nu) \left[(x^i - x^j - a') \ln \left((x^i - x^j - a')^2 + (y^k)^2 \right) - (x^i - x^j + a') \ln \left((x^i - x^j + a')^2 + (y^k)^2 \right) \right] \right. \\ &\quad \left. + (L - x^j + a') \ln(L - x^j + a') - (L - x^j - a') \ln(L - x^j - a') \right\} P_y^j. \end{aligned}$$

2.2. Statement and solving of problem when normal displacement is applied to segment inside half plane

(a) Setting. Let us consider a non-classical problem, when along the entire border of half plane D (see Fig. 1) the tangent stress is equal to zero, and normal displacement u_y on segment $|x| \leq c, y = -b$ lying inside the body is known. Also, normal stress along part $|x| > c, y = 0$ of boundary is equal to zero. Thus, we have the following boundary conditions:

$$\begin{aligned} \text{when } |x| < \infty \text{ and } y = 0: \quad &\sigma_{yx} = 0, \\ \text{when } |x| > c \text{ and } y = 0: \quad &\sigma_{yy} = 0, \\ \text{when } |x| \leq c \text{ and } y = -b: \quad &u_y = -U_0(x), \end{aligned}$$

where $U_0(x)$ is the sufficiently smooth function given along segment $[-c, c]$.

We can formulate this problem as follows: let us find the distribution of normal stress σ_{yy} along part $|x| \leq c, y = 0$ of the boundary of the half plane when normal displacement along segment $|x| \leq c, y = -b$ lying inside half plane D equals to $-U_0(x)$.

Let us consider this function of the following kind $U_0(x) = P \cdot 10^{-|4x|}$, ($P = \text{constant}$), which describes clearly expressed non-uniform normal displacement. Thus, we will have the following localization problem: let us find the distribution of normal stress σ_{yy} along segment A_1B_1 to obtain the pit of a given value along segment AB (displacements localization) (see Fig. 1).

(b) Solution. Let us divide segments $|x| \leq c, y = 0$ and $|x| \leq c, y = -b$ into N segments (elements) with equal $2a$ and smaller lengths. We mean that constant normal stresses P_y^j act on each j^{th} segment of segment $|x| \leq c, y = 0$, each with the length of $2a$ and with centre $(x^j, 0)$. We must find such values of these stresses, for which the values of normal displacement in middle point $(x^i, -b)$ of each i^{th} element with length $2a$ of $|x| \leq c, y = -b$ segment inside the body should equal to the given value of $-U_0(x^i)$.

Normal displacement in the centre of the i^{th} element lying on segment $|x| \leq c, y = -b$ will be computed with the following formula:

$$u_y(x^i, -b) = \sum_{j=1}^N B^{\#} P_y^j, \quad i = 1, 2, \dots, N,$$

where we have the following formula for influence coefficients $B^{\#}$:

$$\begin{aligned} B^{\#} &= \frac{1}{2\pi\mu} \left\{ -b(1-2\nu) \left(\arctan \frac{b}{x^i - x^j - a} - \arctan \frac{b}{x^i - x^j + a} \right) \right. \\ &\quad \left. + (1-\nu) \left[(x^i - x^j - a) \ln \left((x^i - x^j - a)^2 + b^2 \right) - (x^i - x^j + a) \ln \left((x^i - x^j + a)^2 + b^2 \right) \right] \right. \\ &\quad \left. + (L - x^j + a) \ln(L - x^j + a) - (L - x^j - a) \ln(L - x^j - a) \right\}. \end{aligned}$$

Thus, the set problem is reduced to solving the following system of linear algebraic equations (N equations with N unknown values):

$$\sum_{j=1}^N B^j P_y^j = -U_0(x^j), \quad i = 1, 2, \dots, N. \quad (4)$$

If we solve system (4) in relation to unknown values P_y^j , then the set problem can be considered as solved, like the problem set in 2.1.

3. Numerical simulation

By using MATLAB software, we obtained the numerical values of the normal stresses (problem of stresses localization) and displacements (problem of displacements localization) along segment AB (the given normal load and normal displacement) and distribution of normal stresses along segment A_1B_1 (the obtained normal stress) shown in Fig. 1 for the following data: $c=1m, 2m, 3m, 4m, 15m, 18m, 20m, 30m$, and $b=5m, 6,5m, 8m, 10m, 15m, 18m, 20m, 30m$; $N=120$; $P=10kg/cm^2$. Below are graphs of some of the obtained results. Namely, Fig. 2 shows load $P_0(x)$ and Fig. 3, Fig. 4 shows normal displacement $U_0(x)$ along AB segment and distribution of obtained normal stress P_y along A_1B_1 segment, when $c=1m$ and $b=5m, 6,5m, 8m, 10m$.

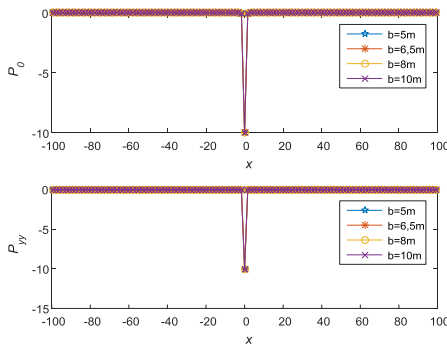


Fig. 2 The load $P_0(x)$ along segment AB and distribution of obtained normal stress $P_{yy} := \sigma_{yy}$ along segment A_1B_1 , when $c=1m$.

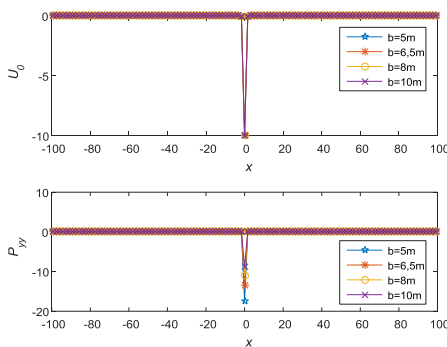


Fig.3 Displacement $U_0(x)$ along segment AB and distribution of obtained normal stress P_{yy} along segment A_1B_1 , when $c=1m$ and $E=2 \times 10^2 kg/cm^2$, $\nu=0.42$ (technical rubber).

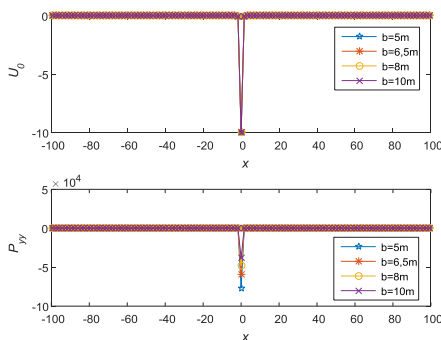


Fig. 4 Displacement $U_0(x)$ along segment AB and distribution of obtained

normal stresses P_{yy} along segment A_1B_1 , when $c=1m$ and $E=2 \times 10^8 kg/cm^2$, $\nu=0.3$ (steel).

Besides, represented 3D graphs of the distribution of stresses and displacements in the body section relevant to domain $-c < x < c, -30 < y < -10$, when $c=1m, b=30m$; for steel $E=2 \times 10^8 kg/cm^2$, $\nu=0.3$ (see Fig. 5 and Fig. 8 for stresses localization problem, and Fig. 6 and Fig. 10 for displacements localization problem) and technical rubber $E=2 \times 10^2 kg/cm^2$, $\nu=0.42$ (see Fig. 9 for stresses localization problem, and Fig.7, Fig.11 for displacements localization problem). Formula (3) evidences that the stresses in the stress problems do not depend on Young's modulus and Poisson's ratio. As for the displacements, the normal displacement less and tangential displacement is bigger in steel than in technical rubber.

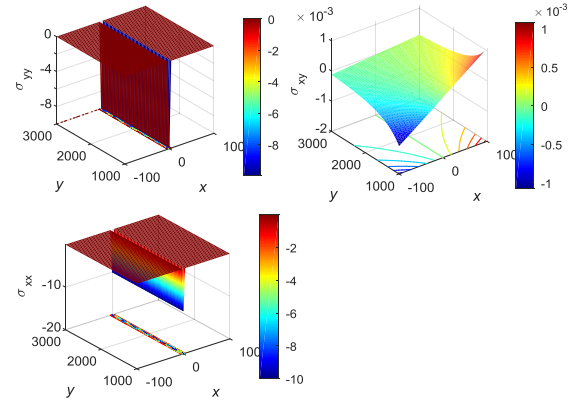


Fig. 5 Distribution of stresses in domain $-c < x < c, -30 < y < -10$, when $c=1m, b=30m, \nu=0.3$ (in stresses for the problem, when $P_0(x) = P \cdot 10^{-|4+x|}$).

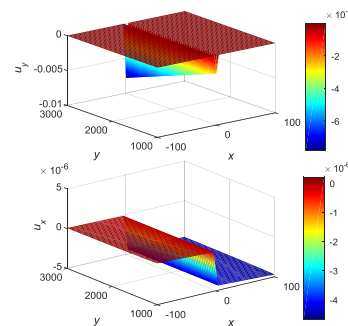


Fig. 6 Distribution of displacements for steel in domain $-c < x < c, -30 < y < -10$, when $c=1m, b=30m, E=2 \times 10^8 kg/cm^2, \nu=0.3$ (in stresses for the problem, when $P_0(x) = P \cdot 10^{-|4+x|}$).

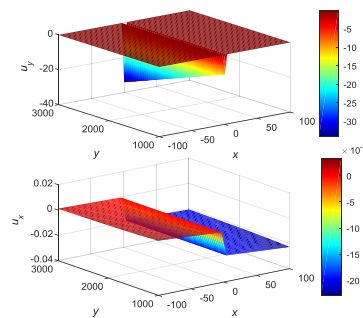


Fig. 7 Distribution of displacements for technical rubber in domain $-c < x < c, -30 < y < -10$, when $c=1m, b=30m, E=2 \times 10^2 kg/cm^2, \nu=0.42$ (in stresses for the problem, when

$$P_0(x) = P \cdot 10^{-14|x|}$$

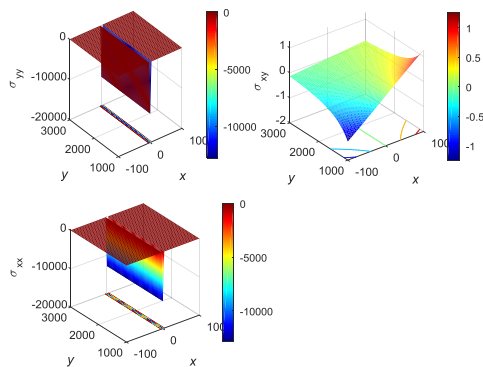


Fig. 8 Distribution of stresses in the part of the body of steel bordered by domain $-c < x < c, -30 < y < -10$, when $c = 1m, b = 30m, E = 2 \times 10^6 \text{ kg/cm}^2, \nu = 0.3$ (in displacements for the problem when $P_0(x) = P \cdot 10^{-14|x|}$).

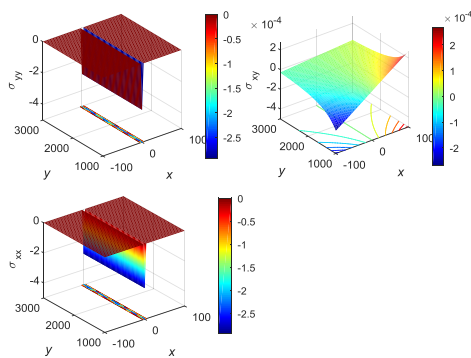


Fig. 9 Distribution of stresses in the part of the body of technical rubber bordered by domain $-c < x < c, -30 < y < -10$, when $c = 1m, b = 30m, E = 2 \times 10^2 \text{ kg/cm}^2, \nu = 0.42$ (in displacements for the problem when $P_0(x) = P \cdot 10^{-14|x|}$).

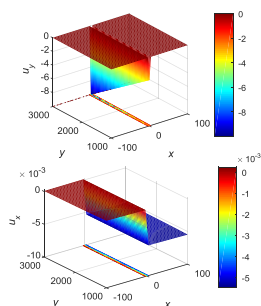


Fig. 10 Distribution of displacements in the part of the body of steel bordered by domain $-c < x < c, -30 < y < -10$, when $c = 1m, b = 30m, E = 2 \times 10^6 \text{ kg/cm}^2, \nu = 0.3$ (in displacements for the problem when $P_0(x) = P \cdot 10^{-14|x|}$).

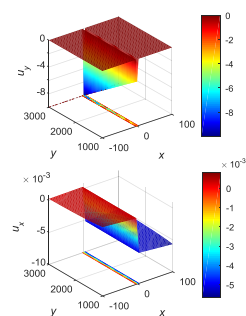


Fig. 11 Distribution of displacements in the part of the body of technical rubber bordered by domain $-c < x < c, -30 < y < -10$, when $c = 1m, b = 30m, E = 2 \times 10^2 \text{ kg/cm}^2, \nu = 0.42$ (in displacements for the

problem when $P_0(x) = P \cdot 10^{-14|x|}$).

4. Conclusion

The paper sets non-classical problems, and problems of localization of stress and displacement for a homogeneous isotropic elastic half-plane are formulated based on them. The essence of the problems is as follows: we must find the distribution of the normal stress along section AB_1 (see Fig. 1) of the border of the half plane so that normal stress σ_y or normal displacement u_y along segment AB parallel to the border of a given length distanced from the border by b within the body should equal to the value of the given function. If we take the kind of this function, which describes the point-force applied to the middle point of section AB (e.g. $U_0(x) = C \cdot 10^{-14|x|}$, ($C = \text{constant}$)), we will obtain the problem of localization of stresses and displacements. The set problems are solved by BEM [1].

By using the MATLAB's software, we obtained the numerical results and plotted the corresponding graphs showing the values of normal stress to be applied to the part of the boundary of the half plane to obtain the point force or displacement in the middle point of a segment inside the body. The paper also presents 3D graphs of distribution of stresses and displacements within the parts of the bodies of steel and technical rubber bordered by domain .

The problems considered in the work can be used in practice, e.g. in soils and rocks, materials that are susceptible to cracking and faulting when sheared, as well materials used to demolish military structures or in underground facilities.

References

- [1] Crouch, S.L., Starfield A.M. Boundary element methods in solid mechanics. Allen & Unwin, London, 1983
- [2] Zirakashvili, N. On the numerical solution of some two-dimensional boundary-contact delocalization problems - Meccanica, 48(7), 2013,1791–1804
- [3] Agalovyan, L.A . The solution asymptotics of classical and nonclassical, static and dynamic boundary-value problems for thin bodies - J Int Appl Mech 38(7), 2002, 765–782
- [4] Dehghan Mehdi. Numerical solution of a non-local boundary value problem with Neumann's boundary conditions - Commun Numer Methods Eng 19(1), 2002, 1–12
- [5] Sladek, J., Sladek, V., Baant, Z.P. Non-local boundary integral formulation for softening damage - Int J Numer Meth Eng 57(1), 2003, 103–116
- [6] Avalishvili, G, Avalishvili, M., Gordeziani, D. On some non-classical two-dimensional models for thermoelastic plates with variable thickness - Bull Georgian Natl Acad Sci (N.S.) 4(2), 2010, 27–34
- [7] Avalishvili, G, Avalishvili, M., Gordeziani, D. On integral nonlocal boundary value problems for some partial differential equations - Bull Georgian Natl Acad Sci (N.S.) 5(1), 2011, 31–37
- [8] Ma, H. M. , Gao, X. -L., Reddy, J. N. A non-classical Mindlin plate model based on a modified couple stress theory - Acta Mechanica 220 (1), 2011, 217–235
- [9] Khomasuridze, N., Janjgava, R., Zirakashvili, N. Some non-classical thermoelasticity problems for a rectangular parallelepiped - Meccanica, 49(6), 2014, 1337-1342
- [10] Zirakashvili, N. Numerical Simulation of Some Non-Classical Elasticity Problems for the Half-Space by the Boundary Element Method - Bulletin of TICMI, 22(1), 2018, 41-58

MODELING OF A CYLINDRICAL BODY MOTION ON A VIBRATING SURFACE

МОДЕЛИРОВАНИЕ ДВИЖЕНИЯ ЦИЛИНДРИЧЕСКОГО ТЕЛА ПО ВИБРИРУЮЩЕЙ ПОВЕРХНОСТИ

Doctor of Physical and Mathematics sciences, Prof. Ibrayev A.,
Candidate of Physical and Mathematics sciences, Assoc. Prof. Bersugir M.
Eurasian National University named after L.N.Gumilev, Nur-Sultan, Kazakhstan
E-mail: ibrayev.askar@mail.ru, bersugir68@mail.ru

Abstract: The problems of continuous motion of a cylindrical body with a displaced center of mass along vibrating horizontal and inclined surfaces are considered.

The analytical solutions of the motion equations were obtained by the method of partial discretization of nonlinear differential equations [1] and graphs of changes in the rotation angles of a cylindrical body were constructed for various cases.

KEY WORDS: SOLID BODY, ROUGH SURFACE, AMPLITUDE, FREQUENCY, MOMENT OF INERTIA, DIFFERENTIAL EQUATIONS

1. Introduction

Vibration processes are widespread in industrial and technological systems. Vibrations are significant in the processes of vibrational movement, transportation, and also used in part process technologies. In general, the dynamics of vibrating machines and mechanisms are widely studied. In studies of vibrational processes, modeling plays a significant role. In this case, models of various levels of complexity are used. The indicated models are reduced to the description of nonlinear differential equations system, the analytical solutions of which present known difficulties. Therefore, the construction of their analytical solutions is very relevant.

2. Preconditions and means for resolving the problem

The movement of a cylindrical body occurs under the action of gravity and the reaction of the surface applied at a point P . Decompose the reaction into two components: vertical N and horizontal F (Fig. 1).

Let the surface perform translational rectilinear harmonic oscillations according to the law $\xi = A \sin(\omega t)$, directed at an angle β to the horizontal

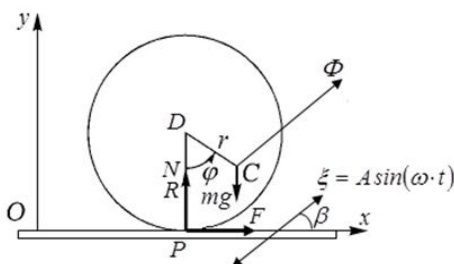


Fig.1 The movement of a cylindrical body on a vibrating horizontal surface

Here: A, ω – amplitude and frequency of oscillations; t – time. The inertial properties of the body are characterized by mass and moment of inertia relative to the center of mass C . We will set the position of the body by the x_C, y_C coordinates of the center of mass in the Oxy coordinate system associated with a rough surface and the rotation angle φ .

The interaction of a solid body with a surface occurs through the action of a normal reaction N and friction force F (rolling friction is neglected). Assume that friction obeys the Amont-Coulomb law:

$$|F| \leq f \cdot N,$$

where f is the coefficient of sliding friction. In this paper, we consider continuous motion, $N \geq 0$.

The body is also under the influence of gravity force mg . In relative motion, to all forces it is necessary to add the portable inertia force:

$$\Phi = m \cdot A \cdot \omega^2 \cdot \sin(\omega t).$$

Non-slip rolling of a cylindrical body with a displaced center of mass on a horizontal surface is described by differential equations system arising from general theorems on the motion of the center of mass and on the change in the kinetic moment [2,3]:

$$\begin{aligned} m\ddot{x}_C &= F + \Phi \cos \beta, \\ m\ddot{y}_C &= N - mg + \Phi \sin \beta, \\ J_C \ddot{\varphi} &= F(R - r \cos \varphi) - Nr \sin \varphi, \end{aligned} \tag{1}$$

where m – mass of a body; x_C, y_C – coordinate of center of mass C of the body; N – normal reaction of the surface; J_C – moment of inertia about an axis perpendicular to the surface of the body; φ – body rotation angle; R – cylinder radius; r – distance from the geometric center to the center of gravity of the body; g – gravitational acceleration.

Consider the system of differential equations (1) together with the initial conditions

$$t=0: \varphi = \varphi_0, \quad \dot{\varphi} = \dot{\varphi}_0. \tag{2}$$

For a more convenient recording, we consider positive the direction of the rotation angle counterclockwise. The coordinates of the center of mass C can be represented as:

$$x_C = x_D + r \sin \varphi; \quad y_C = R - r \cos \varphi, \tag{3}$$

where $x_D, y_D = R$ – coordinates of the center of curvature D , $r = CD$.

When rolling without sliding, the instantaneous center of velocity is at the point of contact P , i.e. $v_P = 0$, or

$$\dot{x}_D = -\dot{\varphi}R; \quad \dot{y}_D = 0. \tag{4}$$

Using (3), (4), find:

$$\begin{aligned} \ddot{x}_C &= -(R - r \cos \varphi) \ddot{\varphi} - r \sin \varphi \cdot \dot{\varphi}^2; \\ \ddot{y}_C &= r \sin \varphi \cdot \ddot{\varphi} + r \cos \varphi \cdot \dot{\varphi}^2. \end{aligned} \tag{5}$$

The first two of the three differential equations of the body motion (1), taking into account (5), give the dependence of the components of the surface reaction on $\varphi, \dot{\varphi}$ и $\ddot{\varphi}$:

$$\begin{aligned} N &= m[g + r(\sin \varphi \cdot \ddot{\varphi} + \cos \varphi \cdot \dot{\varphi}^2)] - mA\omega^2 \sin(\omega t) \sin \beta, \\ F &= -m[(R - r \cos \varphi) \ddot{\varphi} + r \sin \varphi \cdot \dot{\varphi}^2] - mA\omega^2 \sin(\omega t) \cos \beta. \end{aligned} \tag{6}$$

Substituting expressions (6) into the third of the differential equations of motion of the body (1), arrive at the equation describing the change in the rotation angle $\varphi(t)$:

$$\begin{aligned} [J_C + m(R^2 + r^2 - 2Rr \cos \varphi)] \ddot{\varphi} + mrs \sin \varphi (R\dot{\varphi}^2 + g) + \\ + mA\omega^2 \sin(\omega t) [R \cos \beta - r \cos(\varphi - \beta)] = 0. \end{aligned} \tag{7}$$

By entering the notation

$$f(t) = \frac{m}{J_C + m(R^2 + r^2 - 2Rr \cos \varphi)}, \tag{8}$$

obtain equations (7) in the form

$$\ddot{\varphi} + f(t) \{ r \sin \varphi (R\dot{\varphi}^2 + g) + A \cdot \omega^2 \cdot \sin(\omega t) [R \cos \beta - r \cos(\varphi - \beta)] \} = 0. \tag{9}$$

3. Results and discussion

The last equation in its final form is not integrated. To solve problem (9)-(2) using the method of partial discretization of nonlinear differential equations, obtain

$$\begin{aligned} \ddot{\varphi} = -\frac{1}{2} \sum_{i=1}^n (t_i + t_{i+1}) \{ f(t_i) \{ r \sin \varphi(t_i) (R\dot{\varphi}(t_i)^2 + g) + \\ + A \cdot \omega^2 \cdot \sin(\omega t_i) [R \cos \beta - r \cos(\varphi(t_i) - \beta)] \} \delta(t - t_i) - \\ - f(t_{i+1}) \{ r \sin \varphi(t_{i+1}) (R\dot{\varphi}(t_{i+1})^2 + g) + A \cdot \omega^2 \cdot \sin(\omega t_{i+1}) \times \\ \times [R \cos \beta - r \cos(\varphi(t_{i+1}) - \beta)] \} \delta(t - t_{i+1}) \}, \end{aligned} \tag{10}$$

where $\delta(t)$ – Delta Dirac function.

The general solution of equation (10) has the expression

$$\begin{aligned} \dot{\varphi}(t) = C_1 - \frac{1}{2} \sum_{i=1}^n (t_i + t_{i+1}) \{ f(t_i) \{ r \sin \varphi(t_i) (R\dot{\varphi}(t_i)^2 + g) + \\ + A \cdot \omega^2 \cdot \sin(\omega t_i) [R \cos \beta - r \cos(\varphi(t_i) - \beta)] \} H(t - t_i) - \\ - f(t_{i+1}) \{ r \sin \varphi(t_{i+1}) (R\dot{\varphi}(t_{i+1})^2 + g) + A \cdot \omega^2 \cdot \sin(\omega t_{i+1}) \times \\ \times [R \cos \beta - r \cos(\varphi(t_{i+1}) - \beta)] \} H(t - t_{i+1}) \}, \end{aligned} \tag{11}$$

where $H(t)$ – Heaviside function, C_1 – arbitrary integration constant.

Using the initial conditions (2), we have

$$\begin{aligned} \dot{\varphi}(t) = \dot{\varphi}_0 - \frac{1}{2} \sum_{i=1}^n (t_i + t_{i+1}) \{ f(t_i) \{ r \sin \varphi(t_i) (R\dot{\varphi}(t_i)^2 + g) + \\ + A \cdot \omega^2 \cdot \sin(\omega t_i) [R \cos \beta - r \cos(\varphi(t_i) - \beta)] \} H(t - t_i) - \\ - f(t_{i+1}) \{ r \sin \varphi(t_{i+1}) (R\dot{\varphi}(t_{i+1})^2 + g) + A \cdot \omega^2 \cdot \sin(\omega t_{i+1}) \times \\ \times [R \cos \beta - r \cos(\varphi(t_{i+1}) - \beta)] \} H(t - t_{i+1}) \}. \end{aligned} \tag{12}$$

The general solution of equation (12) has the expression

$$\begin{aligned} \dot{\varphi}(t) = \dot{\varphi}_0 t + C_2 - \frac{1}{2} \sum_{i=1}^n (t_i + t_{i+1}) \{ f(t_i) \{ r \sin \varphi(t_i) (R\dot{\varphi}(t_i)^2 + g) + \\ + A \cdot \omega^2 \cdot \sin(\omega t_i) [R \cos \beta - r \cos(\varphi(t_i) - \beta)] \} (t - t_i) H(t - t_i) - \\ - f(t_{i+1}) \{ r \sin \varphi(t_{i+1}) (R\dot{\varphi}(t_{i+1})^2 + g) + A \cdot \omega^2 \cdot \sin(\omega t_{i+1}) \times \\ \times [R \cos \beta - r \cos(\varphi(t_{i+1}) - \beta)] \} (t - t_{i+1}) H(t - t_{i+1}) \}. \end{aligned} \tag{13}$$

With taking into account the initial conditions (2), the solution of equation (13) will have the form

$$\begin{aligned} \varphi(t) = \dot{\varphi}_0 t + \varphi_0 - \frac{1}{2} \sum_{i=1}^n (t_i + t_{i+1}) \{ f(t_i) \{ r \sin \varphi(t_i) (R\dot{\varphi}(t_i)^2 + g) + \\ + A \cdot \omega^2 \cdot \sin(\omega t_i) [R \cos \beta - r \cos(\varphi(t_i) - \beta)] \} (t - t_i) H(t - t_i) - \\ - f(t_{i+1}) \{ r \sin \varphi(t_{i+1}) (R\dot{\varphi}(t_{i+1})^2 + g) + A \cdot \omega^2 \cdot \sin(\omega t_{i+1}) \times \\ \times [R \cos \beta - r \cos(\varphi(t_{i+1}) - \beta)] \} (t - t_{i+1}) H(t - t_{i+1}) \}. \end{aligned} \tag{14}$$

In accordance with equation (14), expressions of the rotation angle $\varphi(t_k)$ and the angular velocity $\dot{\varphi}(t_k)$ of the body at times t_k will be:

$$\begin{aligned} \varphi(t_1) &= \dot{\varphi}_0 t_1 + \varphi_0; \\ \dot{\varphi}(t_1) &= \dot{\varphi}_0 - \frac{1}{2} (t_1 + t_2) f(t_1) \{ r \sin \varphi(t_1) (R\dot{\varphi}(t_1)^2 + g) + \\ &+ A \cdot \omega^2 \cdot \sin(\omega t_1) [R \cos \beta - r \cos(\varphi(t_1) - \beta)] \}; \\ \varphi(t_2) &= \dot{\varphi}_0 t_2 + \varphi_0 - \frac{1}{2} (t_1 + t_2) f(t_1) \{ r \sin \varphi(t_1) (R\dot{\varphi}(t_1)^2 + g) + \\ &+ A \cdot \omega^2 \cdot \sin(\omega t_1) [R \cos \beta - r \cos(\varphi(t_1) - \beta)] \} (t_2 - t_1); \\ \dot{\varphi}(t_2) &= \dot{\varphi}_0 - \frac{1}{2} (t_1 + t_2) f(t_1) \{ r \sin \varphi(t_1) (R\dot{\varphi}(t_1)^2 + g) + A \cdot \omega^2 \cdot \sin(\omega t_1) \} + \\ &+ [R \cos \beta - r \cos(\varphi(t_1) - \beta)] - \frac{1}{2} (t_3 - t_1) f(t_2) \{ r \sin \varphi(t_2) (R\dot{\varphi}(t_2)^2 + g) + \\ &+ A \cdot \omega^2 \cdot \sin(\omega t_2) [R \cos \beta - r \cos(\varphi(t_2) - \beta)] \}; \\ \varphi(t_3) &= \dot{\varphi}_0 t_3 + \varphi_0 - \frac{1}{2} (t_1 + t_2) f(t_1) \{ r \sin \varphi(t_1) (R\dot{\varphi}(t_1)^2 + g) + \\ &+ A \cdot \omega^2 \cdot \sin(\omega t_1) [R \cos \beta - r \cos(\varphi(t_1) - \beta)] \} (t_3 - t_1) - \\ &- \frac{1}{2} (t_3 - t_1) f(t_2) \{ r \sin \varphi(t_2) (R\dot{\varphi}(t_2)^2 + g) + A \cdot \omega^2 \cdot \sin(\omega t_2) \times \\ &\times [R \cos \beta - r \cos(\varphi(t_2) - \beta)] \} (t_3 - t_2) - \frac{1}{2} (t_4 - t_2) f(t_3) \times \\ &\times \{ r \sin \varphi(t_3) (R\dot{\varphi}(t_3)^2 + g) + A \cdot \omega^2 \cdot \sin(\omega t_3) \} \times \\ &\times [R \cos \beta - r \cos(\varphi(t_3) - \beta)] (t_3 - t_2); \end{aligned}$$

$$\begin{aligned} \dot{\varphi}(t_3) = & \dot{\varphi}_0 - \frac{1}{2}(t_1 + t_2)f(t_1)\{r\sin\varphi(t_1)(R\dot{\varphi}(t_1)^2 + g) + \\ & + A \cdot \omega^2 \cdot \sin(\omega t_1)[R\cos\beta - r\cos(\varphi(t_1) - \beta)]\} - \\ & - \frac{1}{2}(t_3 - t_1)f(t_2)\{r\sin\varphi(t_2)(R\dot{\varphi}(t_2)^2 + g) + A \cdot \omega^2 \cdot \sin(\omega t_2) \times \\ & \times [R\cos\beta - r\cos(\varphi(t_2) - \beta)]\} - \frac{1}{2}(t_4 - t_2)f(t_3) \times \\ & \times \{r\sin\varphi(t_3)(R\dot{\varphi}(t_3)^2 + g) + A \cdot \omega^2 \cdot \sin(\omega t_3) \times \\ & \times [R\cos\beta - r\cos(\varphi(t_3) - \beta)]\} \end{aligned}$$

Using the method of mathematical induction, construct analytical expressions of the rotation angle $\varphi(t_k)$ and the angular velocity $\dot{\varphi}(t_k)$ at an arbitrary point $k = \overline{1, n}$:

$$\begin{aligned} \varphi(t_k) = & \dot{\varphi}_0 t_k + \varphi_0 - \frac{1}{2}(t_1 + t_2)f(t_1)\{r\sin\varphi(t_1)(R\dot{\varphi}(t_1)^2 + g) + \\ & + A \cdot \omega^2 \cdot \sin(\omega t_1)[R\cos\beta - r\cos(\varphi(t_1) - \beta)]\}(t_k - t_1) - \\ & - \frac{1}{2} \sum_{i=2}^k (t_{i+1} - t_{i-1})f(t_i)\{r\sin\varphi(t_i)(R\dot{\varphi}(t_i)^2 + g) + \\ & + A \cdot \omega^2 \cdot \sin(\omega t_i)[R\cos\beta - r\cos(\varphi(t_i) - \beta)]\}(t_k - t_i), \\ (15) \quad \dot{\varphi}(t_k) = & \dot{\varphi}_0 - \frac{1}{2}(t_1 + t_2)f(t_1)\{r\sin\varphi(t_1)(R\dot{\varphi}(t_1)^2 + g) + \\ & + A \cdot \omega^2 \cdot \sin(\omega t_1)[R\cos\beta - r\cos(\varphi(t_1) - \beta)]\} - \\ & - \frac{1}{2} \sum_{i=2}^k (t_{i+1} - t_{i-1})f(t_i)\{r\sin\varphi(t_i)(R\dot{\varphi}(t_i)^2 + g) + \\ & + A \cdot \omega^2 \cdot \sin(\omega t_i)[R\cos\beta - r\cos(\varphi(t_i) - \beta)]\} \end{aligned}$$

Figure 2 presents graphs of changes of the rotation angle $\varphi(t)$ of a cylindrical body located on a horizontal surface. System parameters correspond to the values: $m = 50 \text{ kg}$, $\beta = 0,524 \text{ rad}$, $R = 0,5 \text{ m}$, $\varphi(0) = 0,175 \text{ rad}$, $\dot{\varphi}(0) = 0$.

In this case, the center of mass of the cylindrical body is offset from the geometric center by half the radius, i.e. $r = 0,25 \text{ m}$.

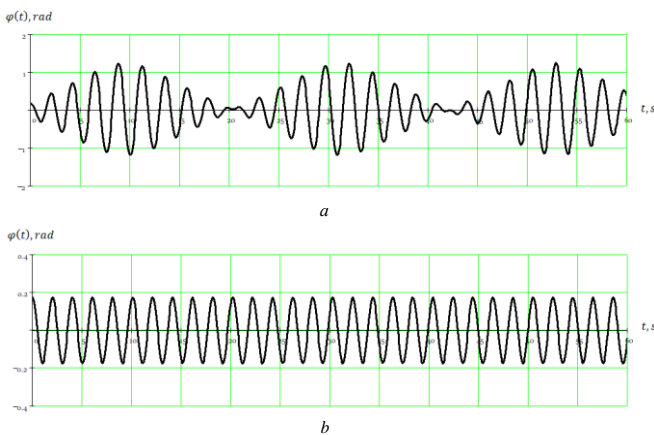


Fig.2 Graphs of changes of the rotation angle $\varphi(t)$:

a) at $A = 0,1 \text{ m}$, $\omega = 3 \text{ rad/s}$; b) at $A = 0,001 \text{ m}$, $\omega = 10 \text{ rad/s}$

From graph 2a it follows that the nature of the beating occurs with the corresponding parameters $A = 0,1 \text{ m}$, $\omega = 3 \text{ rad/s}$.

Figure 2b shows a graph of changes $\varphi(t)$ at $A = 0,001 \text{ m}$, $\omega = 10 \text{ rad/s}$. As follows from this graph, the fluctuations of the rotation angle $\varphi(t)$ obeys the harmonic law and has an established character. It should be noted that when $r < 0,25 \text{ m}$, the period of oscillation of the rotation angle increases, when $r > 0,25 \text{ m}$ the period decreases.

Consider the motion of a cylindrical solid with a displaced center of mass along a vibrating inclined surface (Fig. 3).

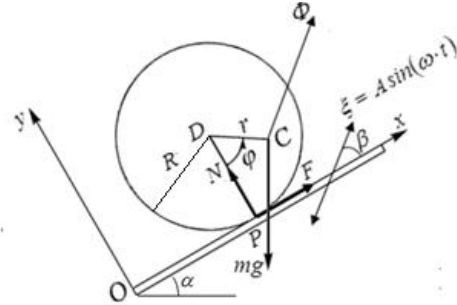


Fig.3 The motion of a cylindrical solid on a vibrating inclined surface

In this case, the system of differential equations (1) takes the following form

$$\begin{aligned} m\ddot{x}_C = & F + \Phi\cos\beta - mg\sin\alpha, \\ (16) \quad m\ddot{y}_C = & N + \Phi\sin\beta - mg\cos\alpha, \\ J_C\ddot{\varphi} = & F(R - r\cos\varphi) - Nr\sin\varphi. \end{aligned}$$

After some transformations, from the system of differential equations (16) obtain the values of the surface reaction components from φ , $\dot{\varphi}$ и $\ddot{\varphi}$ in the form

$$\begin{aligned} N = & mr(\sin\varphi \cdot \ddot{\varphi} + \cos\varphi \cdot \dot{\varphi}^2) - mA\omega^2 \sin(\omega t)\sin\beta + mg\cos\alpha, \\ (17) \quad F = & -m[(R - r\cos\varphi)\ddot{\varphi} + r\sin\varphi \cdot \dot{\varphi}^2] - mA\omega^2 \sin(\omega t)\cos\beta + mgsin\alpha. \end{aligned}$$

Substituting expressions (17) into the third of the system of differential equations of body motion (16) and introducing the notation (8), obtain the expression for the change in the rotation angle $\varphi(t)$ in time:

$$\begin{aligned} \ddot{\varphi} + f(t)\{rR\sin\varphi\dot{\varphi}^2 - g[R\sin\alpha - r\sin(\varphi + \alpha)] + A \cdot \omega^2 \cdot \sin(\omega t) \times \\ (18) \quad \times [R\cos\beta - r\cos(\varphi - \beta)]\} = 0. \end{aligned}$$

Similarly, by the above method, obtain an analytical solution in the form:

$$\begin{aligned} \varphi(t) = & \dot{\varphi}_0 t + \varphi_0 - \frac{1}{2} \sum_{i=1}^n (t_i + t_{i+1}) \{f(t_i)\{rR\sin\varphi(t_i)\dot{\varphi}^2(t_i) + A\omega^2 \times \\ & \times \sin(\omega t_i)[R\cos\beta - r\cos(\varphi(t_i) - \beta)] - g[R\sin\alpha - r\sin(\varphi(t_i) + \alpha)]\} \times \\ (19) \quad \times (t - t_i)H(t - t_i) - f(t_{i+1})\{rR\sin\varphi(t_{i+1})\dot{\varphi}^2(t_{i+1}) + A\omega^2 \sin(\omega t_{i+1}) \times \\ & \times [R\cos\beta - r\cos(\varphi(t_{i+1}) - \beta)] - g[R\sin\alpha - r\sin(\varphi(t_{i+1}) + \alpha)]\} \times \\ & \times (t - t_{i+1})H(t - t_{i+1})\}. \end{aligned}$$

Using the same transformations, define the expressions of the rotation angle $\varphi(t_k)$ and the angular velocity $\dot{\varphi}(t_k)$ of the body at times t_k in the following form

$$\begin{aligned}
 \varphi(t_k) &= \dot{\varphi}_0 t_k + \varphi_0 - \frac{1}{2}(t_1 + t_2) f(t_1) \{r R \sin \varphi(t_1) \dot{\varphi}^2(t_1) + \\
 &+ A \omega^2 \sin(\omega t_1) [R \cos \beta - r \cos(\varphi(t_1) - \beta)] - \\
 &- g [R \sin \alpha - r \sin(\varphi(t_1) + \alpha)]\} (t_k - t_1) - \frac{1}{2} \sum_{i=2}^k (t_{i+1} - t_{i-1}) f(t_i) \times \\
 &\times \{r R \sin \varphi(t_i) \dot{\varphi}^2(t_i) + A \omega^2 \sin(\omega t_i) [R \cos \beta - r \cos(\varphi(t_i) - \beta)] - \\
 &- g [R \sin \alpha - r \sin(\varphi(t_i) + \alpha)]\} (t_k - t_i), \\
 (20) \quad \dot{\varphi}(t_k) &= \dot{\varphi}_0 - \frac{1}{2}(t_1 + t_2) f(t_1) \{r R \sin \varphi(t_1) \dot{\varphi}^2(t_1) + A \omega^2 \sin(\omega t_1) \times \\
 &\times [R \cos \beta - r \cos(\varphi(t_1) - \beta)] - g [R \sin \alpha - r \sin(\varphi(t_1) + \alpha)] - \\
 &- \frac{1}{2} \sum_{i=2}^k (t_{i+1} - t_{i-1}) f(t_i) \{r R \sin \varphi(t_i) \dot{\varphi}^2(t_i) + A \omega^2 \sin(\omega t_i) \times \\
 &\times [R \cos \beta - r \cos(\varphi(t_i) - \beta)] - g [R \sin \alpha - r \sin(\varphi(t_i) + \alpha)]\} (t_k - t_i).
 \end{aligned}$$

Figure 3 shows the case when the inclination of the vibrating surface makes an angle with the horizontal: $\alpha = 0,130 \text{ rad}$, other parameters correspond to the values indicated in the previous case.

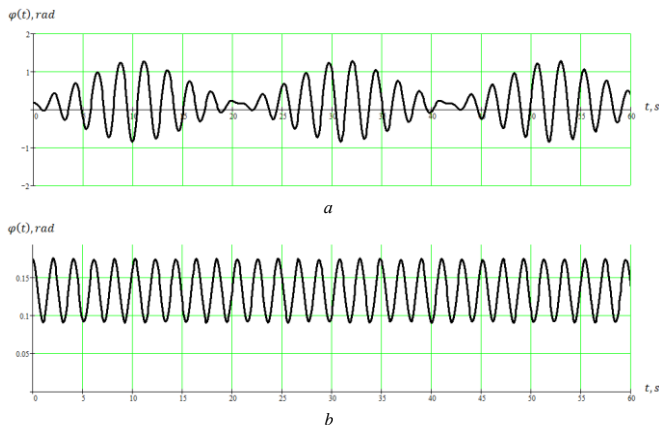


Fig.3 Graphs of changes of the rotation angle $\varphi(t)$:
 a) at $A = 0,1 \text{ m}$, $\omega = 3 \text{ rad/s}$; b) at $A = 0,001 \text{ m}$, $\omega = 10 \text{ rad/s}$

As can be seen from graph 3a, oscillations having the nature of a beating are preserved.

As follows from graph 3b, the oscillations are harmonic, but due to the angle of inclination of the plane, the graph has the form of an offset.

The research results show and this is evident from the graphs.

5. Conclusion

The problems of continuous motion of a cylindrical body with a displaced center of mass along vibrating horizontal and inclined surfaces are considered.

The analytical solutions of the motion equations are obtained by the method of partial discretization of nonlinear differential equations.

Graphs of changes of the rotation angles $\varphi(t)$ of a cylindrical body are constructed for various cases of changing the system parameters.

In particular, changes were made to the distances of the displacement of the center of mass from the geometric center within $r = 0,1 \text{ m}$ до $r = 0,4 \text{ m}$.

It has been established that the nature of the oscillatory processes when the center of mass of the cylindrical body is displaced from the geometric center is significantly affected by the amplitude and frequency of the oscillations.

It is shown that changes in the angle of inclination of the vibrating surface do not significantly affect the rotation angle of the body.

6. Literature

1. Tyurehodzhaev A.N. *Analytical solutions of nonlinear equations and differential equations with variable coefficients*. Proceedings of the «Actual Problems of Mechanics and Engineering» IV International Scientific Conference, II, Almaty, 40-57 (2014).
2. Yelisseyev A.V., Selviskiy V.V., Yelisseyev S.V. *Dynamics of vibrational interactions of elements of technological systems, taking into account unstable bonds: monograph*. – Irkutsk: IrSTU, 2015. – 400 p.
3. Markeev A.P. *Theoretical Mechanics: A manual for Universities*. - Moscow: CheRo, 1999.

APPLICATION OF PERSISTENT HOMOLOGY ON BIO-MEDICAL DATA – A CASE STUDY

Eng. Sekuloski, P., Ass. Prof. Dr. Dimitrievska Ristovska, V.
 Faculty of Computer Science and Engineering, "Ss. Cyril and Methodius" University, Skopje, Macedonia
 petar.sekuloski@finki.ukim.mk, vesna.dimitrievska.ristovska@finki.ukim.mk,

Abstract: In this paper we introduce, analyze and apply persistent homology, one of the main algorithms of TDA, on some real data sets from the bio-medical field. Topological data analysis (TDA) is a field which is a synergy between mathematics, data science and computer science. The main goal of TDA is studying the shape of data using topological techniques. TDA proposes new algorithms that deal with these problems based on tools or concepts from algebraic topology and pure mathematics. We analyze the results and give a topological characterization of the dataset and propose to use them in future work.

Keywords: PERSISTENT HOMOLOGY, TOPOLOGICAL DATA ANALYSIS, ALGEBRAIC TOPOLOGY, DATA SCIENCE, COMPUTATIONAL TOPOLOGY

1. Introduction

Topology is a mathematical field that studies properties of topological spaces, such as connectedness and compactness, invariant of continuous deformations. Algebraic topology studies topological spaces using techniques from algebra by associating algebraic objects such as groups with topological spaces. One of the main tools of algebraic topology is homology. Homology is a mathematical tool which associates sequences of algebraic objects with topological spaces. One way to study a topological space is to find and compute its homology groups. The motivation behind defining homology groups was that two shapes can be distinguished by examining their holes. For example, a disk is different from a circle, or a disk is not a circle, because the disk is solid while the circle has a hole through it. Homology groups are set of invariants of a topological space. These invariants characterize the topological space. The number of structures for some dimension k is the rank of the k -dimensional homology group of the topological space. The number of such structures is known as a Betti number (β_k) of dimension k .

The main idea of Topological Data Analysis is application of these mathematical concepts on real data. Persistent homology is an algorithm from TDA that use homology as main idea. The algorithm computes topological features of a space.

2. Mathematical Background

The starting point is to construct a topological space from a given dataset. We will define some necessary mathematical concepts.

Definition 1. A k -simplex is a convex hull of $k + 1$ affinely independent points $S = \{x_0, x_1, \dots, x_k\} \subseteq \mathbb{R}^d$. The points of S are vertices of the simplex.

The low dimensional simplices (plural: simplices or simplexes) have special names:

- a 0-simplex is called a *vertex*;
- a 1-simplex is called an *edge*;
- a 2-simplex is called a *triangle*;

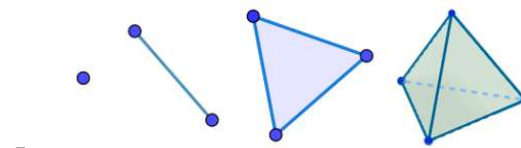


Figure 1. 0-simplex 1-simplex, 2-simplex, 3-simplex

Definition 2. Let σ be a k -simplex defined on $S = \{x_0, x_1, \dots, x_k\}$. A simplex τ defined by $T \subseteq S$ is a face of σ and has σ as a coface. The relationship is denoted with $\sigma \geq \tau$ and $\tau \leq \sigma$.

Definition 3. Let K be a set. Simplicial complex S is a collection of subsets of K called simplices such that:

1. For all $x \in K, \{x\} \in S$.
2. If $\tau \subseteq \sigma \in S$, then $\tau \in S$.

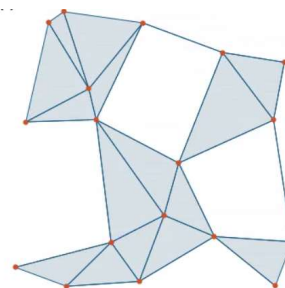


Figure 2. An example of a simplicial complex

We call the sets $\{x\}$ the vertices of K . **Definition 3** gives a more abstract definition of simplicial complex that can be applied to a data where vertices will be the data points. Topological invariants of the space, such as holes and number of connected components, can be computed from a simplicial complex, see Figure 2. One of the key ideas of TDA is to construct a simplicial complex from a dataset. There are a few ways to construct such a simplicial complex [1]. In other words simplicial complexes are high dimensional analogues of graphs. We will explain the steps of the process.

1. Construction of a topological space from a given point cloud

The open (metric) ball of radius $\epsilon > 0$ centered at a point $m \in M$, usually denoted by $B(m; \epsilon)$ is defined by

$$B(m; \epsilon) = \{n \in M \mid d(m, n) \leq \epsilon\}$$

formation of a connected component in the simplicial complex at

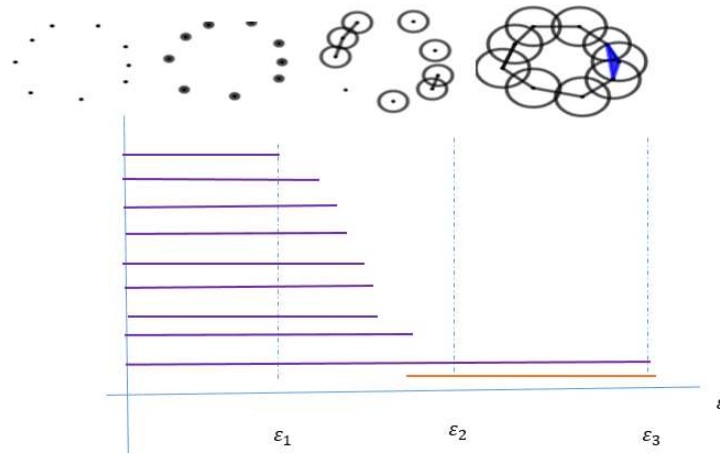


Figure 3. An example of Vietoris-Rips filtration of a space. There are different complexes for different values for ϵ . Violet horizontal lines shows barcodes in dimension 0 and orange line shows barcode for dimension 1.

Let M be a point cloud in \mathbb{R}^d and $\epsilon > 0$. The ϵ -neighborhood of the point cloud M is the set $S(m; \epsilon)$, defined as

$$S(m; \epsilon) = \bigcup_{n \in M} B(m, \epsilon), \quad \epsilon \geq 0.$$

It is known that every ϵ -neighborhood is a topological space. PH gives a summary of a sequence of such topological spaces for different values for ϵ . The key idea here is to see how topological characteristics are changing and which features are the same as ϵ increases.

2. Construction of a simplicial complex from topological space

In our experiments we will use Vietoris-Rips complexes. For a given point cloud M and $\epsilon \geq 0$ we construct Vietoris-Rips complex denoted as $VR(M; \epsilon)$. $VR(M; \epsilon)$ is defined as:

$$VR(M; \epsilon) = \bigcup_{n \geq 0} VR(M; \epsilon)_n$$

$$VR(M; \epsilon)_n = \{(m_0, \dots, m_n) \mid d(m_i, m_j) \leq \epsilon, \text{ for all } i, j \in \{1, 2, \dots, n\}\}$$

Note that $VR(M; \epsilon)_n$ is the set of all n -simplexes of the simplicial complex. The simplicial complex constructed from the topological space is the approximation of the topological space. Hence, every simplicial complex is a topological space which is why we can analyze its topological features.

3. Computing and representing homology groups

Linear algebra is used for computing homology groups of a given simplicial complex. The k^{th} homology group $H_k(S)$ of a simplicial complex S is defined as abelian quotient group. The rank of the H_k , $rank(H_k(S))$, is called k^{th} Betti number of S . It gives a measure of the number of k -dimensional holes in S . The homology groups are computed for every simplicial complex derived from the topological space for each ϵ . Thus, by increasing ϵ we can trail elements of homology groups of the corresponding complex $VR(M; \epsilon)$. We can visualize the existence of homology groups as ϵ increases using a persistent barcode. Persistent barcode is a topological summary of a topological space. When an element shows at some ϵ , we say that an element is born and denote that ϵ as ϵ_{birth} . When the element disappears at some ϵ (it is mapped to 0), we say that the element has died and we denote that ϵ as ϵ_{death} . Every element is represented with a "bar" (a line in the persistent barcode) on the interval $[\epsilon_{birth}, \epsilon_{death}]$. For example, in H_0 , this will correspond to the

ϵ_{birth} and connecting that component with others in a way that they will form a circle in ϵ_{death} , see Figure 3. If we observe the Figure 3, we can see that the orange line is a bar which corresponds to an element of a homology group of dimension 1, which appears near ϵ_2 . It clearly be seen that there is one circle at the last simplex. Also, we can see that near ϵ_2 there is one violet line which means that we have one connected component which corresponds with the given simplex.

3. Diabetes datasets

For this case study we picked two diabetes datasets. First dataset is the Miller-Reaven dataset. Reaven and Miller (1979) examined the relationship among blood chemistry measures of glucose tolerance and insulin in 145 non-obese adults [10]. They used the PRIM9 system to visualize the data in 3D, and discovered a peculiar pattern that looked like a large blob with two wings in different directions. In this dataset, the data is split up in three categories. Data from non-diabetic patients, data from patients with diabetes classified as overt and data from patients with diabetes classified as chemical diabetes. Overt diabetes is the most advanced stage, characterized by elevated fasting blood glucose concentration and classical symptoms. Preceding overt diabetes is the latent or chemical diabetic stage, with no symptoms of diabetes but demonstrable abnormality of oral or intravenous glucose tolerance. There are 145 observations on the following 6 variables:

relwt

relative weight, expressed as the ratio of actual weight to expected weight, given the person's height, a numeric vector

glufast

fasting plasma glucose level, a numeric vector

glutest

test plasma glucose level, a measure of glucose intolerance, a numeric vector

instest

plasma insulin during test, a measure of insulin response to oral glucose, a numeric vector

sspg

steady state plasma glucose, a measure of insulin resistance, a numeric vector

group

diagnostic group, a factor with levels Normal, Chemical_Diabetic, Overt_Diabetic.

4. Preliminary results and discussion

First, we apply persistent homology for each diabetic group of data. For the Chemical_Diabetic group the results are given in Figure 4 and for Overt_Diabetic group the results are given in Figure 5.

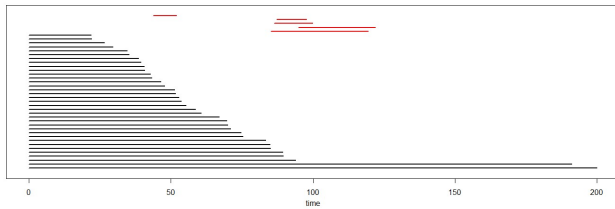


Figure 4. Persistent barcode for the Chemical_Diabetic group

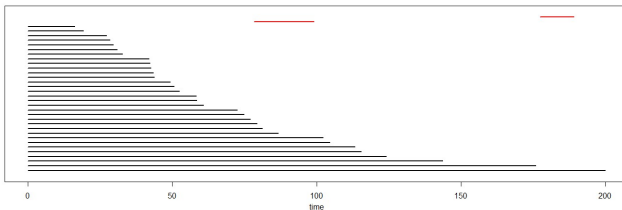


Figure 5. Persistent barcode for the Overt_Diabetic group

We can see that the persistent barcodes are different. In Figure 4, the persistent barcode has more red bars, which means that there are more circles in the simplex constructed from the data for the Chemical_Diabetic group. In this case, there is significant topological difference in the simplexes which means the shape of the data of the two groups is different. A question that arises here is which physical or real factor makes the difference? These factors may be crucial for better understanding the different types of diabetes.

Next, we apply persistent homology on both the diabetic group and the non-diabetic group. The results are given in Figure 6 and Figure 7.

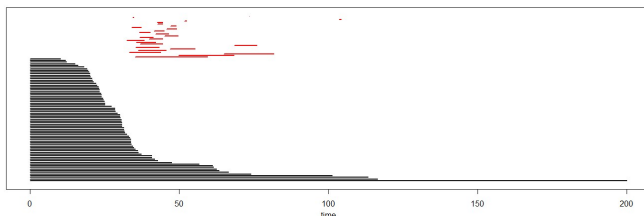


Figure 6. Persistent for non-diabetic group

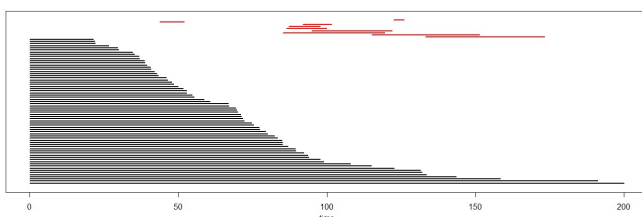


Figure 7. Persistent for diabetic groups

According to the barcodes in Figure 6 and Figure 7, we can conclude that topological characteristics in the data of diabetic and non-diabetic groups are obvious. In the second persistent barcode, there are circles which are present most of the time.

We apply persistent homology on the second dataset which contains data from diabetic and non-diabetic patients. This dataset is originally from the National Institute of Diabetes and Digestive and Kidney Diseases. The objective of the dataset is to diagnostically predict whether or not a patient has diabetes based on certain diagnostic measurements included in the dataset. Several constraints were placed on the selection of these instances from a larger database. In particular, all patients in this dataset are females at least 21 years old and of Pima Indian heritage. The results are given in Figure 8 and Figure 9.

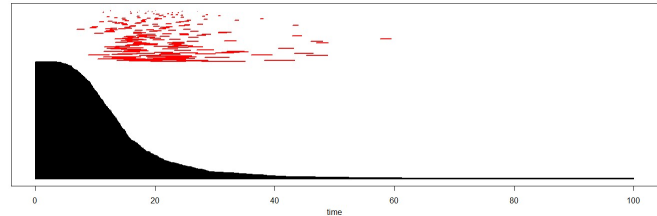


Figure 8. Persistent barcode for non-diabetic data

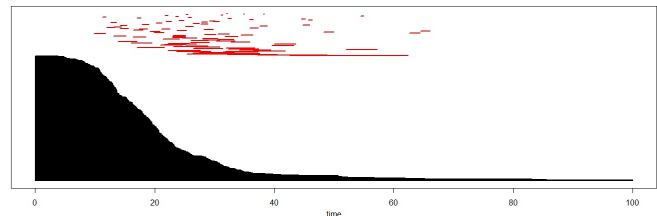


Figure 9. Persistent barcode for diabetic data

5. Further work and application in bio-medical field

The main goal is to link the differences of the topological characterizations of the two types of diabetes to real factors. Persistent homology, and in general, TDA, can be applied in the bio-medical field in many areas. The application of statistics allowed significant progress in understanding diseases. Knowing that, and the fact that TDA gives a new way of analyzing the data, specifically, analyzing the shape of the data, we think that TDA will be useful for medicine. It can be used to see how one factor changes the topological characteristics of the topological space underneath the given data, and how it is related to a disease. If we work in three dimensional Euclidean space, we may find some structural deformations of a system in the body. For example, to observe the deformations of the vasculature of some organ or tissue. In the future, we will investigate how persistent homology can be applied to characterize retinal and liver vasculature networks. TDA can also be applied on big data from the healthcare field.

6. Acknowledgement

This work was partially financed by the Faculty of Computer Science and Engineering at the “Ss. Cyril and Methodius University”, Skopje.

References

- [1] H. Edelsbrunner, "Persistent homology: theory and practice", 2014.
- [2] Gunnar Carlsson, "Topology and data". *Bulletin of the American Mathematical Society*. 46 (2), 2009, pp. 255–308.
- [3] J. R. Munkres, *Topology*. vol. 2. Upper Saddle River: Prentice Hall, 2000
- [4] Ilen Hatcher, *Algebraic topology*. Cambridge University Press, 2002
- [5] G. Carlsson, A. Zomorodian, A. Collins, L. Guibas, J. (2005-12-01). "Persistence barcodes for shapes". *International Journal of Shape Modeling*.
- [6] Brittany Terese Fasy, Jisu Kim, Fabrizio Lecci, and Clément Maria. "Introduction to the r package tda. ", arXiv preprint arXiv:1411.1830, 2014.
- [7] <https://s3.amazonaws.com/cdn.ayasdi.com/wp-content/uploads/2018/11/12131418/TDA-Based-Approaches-to-Deep-Learning.pdf>
- [8] <https://en.wikipedia.org/wiki/Fluoroscopy>
- [9] Ulrich Bauer and Michael Lesnick." Induced matchings of barcodes and the algebraic stability of persistence. In *Proceedings of the thirtieth annual symposium on Computational geometry*", p. 355, 2014.
- [10] Reaven, G. M. and Miller, R. G. (1979). An attempt to define the nature of chemical diabetes using a multidimensional analysis. *Diabetologia*, 16, 17-24.
- [11] A. J. Zomorodian, *Topology for Computing*, Cambridge, 2005
- [12] J. Nicponski and J.-H. Jung, *Topological data analysis of vascular disease: A theoretical framework*, BioRxiv, (2019), p. 637090.
- [13] D. Cohen-Steiner, H. Edelsbrunner, and J. Harer, *Stability of persistence diagrams*, *Discrete & Computational Geometry*, (2007), pp. 103–120
- [14] A. Zomorodian and G. Carlsson, *Computing persistent homology*, *Discrete & Computational Geometry*, 33 (2005), pp. 249–274

MULTIPARAMETER HYBRID NEURAL NETWORK METAMODEL OF EDDY CURRENT PROBES WITH VOLUMETRIC STRUCTURE OF EXCITATION SYSTEM

Trembovetska R., PhD Eng., Assoc. Prof. ; Halchenko V., Dr.Sc. Eng., Prof. ; Tychkov V., PhD Eng., Assoc. Prof.
 Faculty of Electronic Technologies and Robotics – Cherkasy State Technological University, Ukraine

r.trembovetska@chdtu.edu.ua

Abstract: A multiparameter metamodel of the eddy current probe with the volumetric excitation structure is constructed. As variable parameters of the metamodel, the spatial coordinates of the testing zone, the radii of the excitation coils and the height of their location above the testing object were used. Due to the use of hybrid construction of multiple neural networks using decomposition of the search space, an acceptable metamodel’s error of the eddy current probe with volumetric excitation structure is obtained.

Keywords: EDDY CURRENT PROBE, UNIFORM SENSITIVITY, VOLUMETRIC EXCITATION STRUCTURE, EDDY CURRENTS DENSITY, NEURAL NETWORKS, HYBRID RBF-METAMODEL

1. Introduction

Some difficulties associated with the non-uniform sensitivity of the probe in the testing zone are characteristic for the defectometry problems solution by the eddy current method. The non-uniform sensitivity is due to the exponential eddy currents density distribution (ECDD) in the testing object (TO) and is inherent in any type of excitation coils, so their using in this case is not effective. In defectometry the best sensitivity characteristic in the testing zone is considered to be uniform, the so-called P-shaped. In this case, the effect of the dependence of the probe sensitivity to the location of the defect in the testing zone is reduced. Thus, there is a need to create eddy current probes (ECP) with uniform sensitivity, and, consequently, the uniform ECDD in the TO zone. One of the ways to solve this kind of problem is the optimal surrogate synthesis of the excitation system (ES) of ECP. Using parametric non-linear synthesis, a sectioned excitation coil system is created and takes into account the shape, electrophysical parameters of the TO and a priori given uniform sensitivity characteristic.

In [1] the problem of the linear synthesis of ECP with a given structure of the excitation field in the TO zone is considered. In addition, since the linear values of the ECDD were obtained with the help of linear synthesis, the practical implementation of such ECP’s is complicated. The cases, when the given field structure is obtained with non-linear parameters of the probe are not considered in these work.

The non-linear synthesis problem was solved in [2]. The problem solution for the optimal placement of the section coils and their geometric dimensions provided the fixed value of the excitation current density in them is obtained. The structural-parametric synthesis method of the source of the electromagnetic field [3] allows us to solve the problem of choosing the structure of the ES ECP. However, the presence of a conductive medium and the speed effect, i.e. at motionless ECP relatively TO is not taken into account.

2. Background and means to solve the problem

A number of works by the authors of [4–6] are devoted to solving the problems of the non-linear, in the general case, synthesis of non-coaxial circular EDP’s with a planar ES structure. A characteristic feature of a planar ES structure is the presence of M coils of radii $r_k (k = 1...M)$ with their uniform $\Delta r = const$ or non-uniform $\Delta r = var$ arrangement, which are at the same height z_0 above the TO [7] and switched on counter or consensually “across the field” (Fig. 1). For such task the synthesis parameters are three variables $J=f(x, y, r)$: spatial coordinates x, y of the testing zone and the radii of the excitation coil sections r .

Moreover, the obtained ES of planar design with a uniform or un-uniform arrangement of coils provides a value of the reduced error in the uniform of the ECDD in the testing zone from 9 to

11 %, which is not an entirely acceptable result, and leaves the desire to further improve the structure of the ES [4-8].

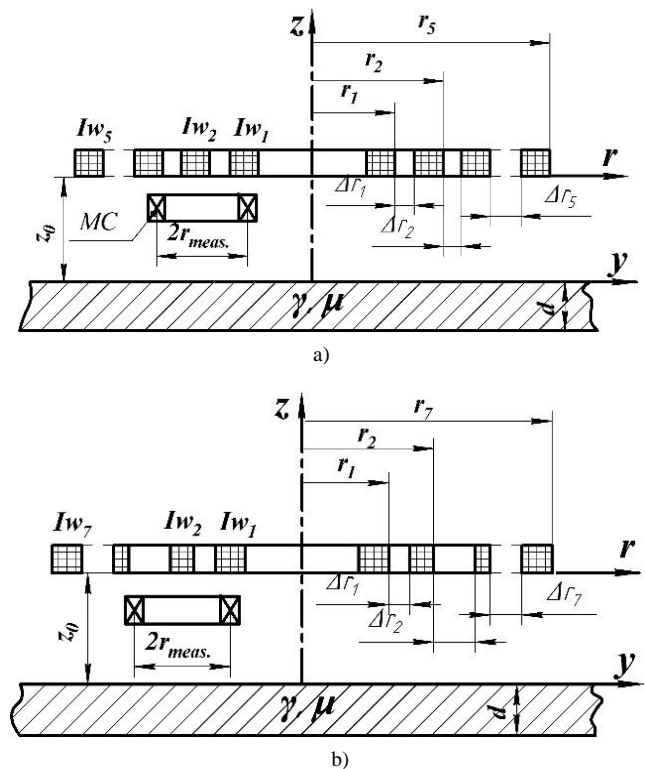


Fig. 1 Variants of the arrangement of the coil sections of the surface ECP with a planar ES structure: a) uniform $\Delta r = const$; b) un-uniform $\Delta r = var$; MC - measuring coil

3. The solution to the problem

As a result, there is a need to study probes with a volumetric structure of ES, both of a homogeneous and heterogeneous structure (Fig. 2).

The arrangement of coils of surface ECP’s of a volumetric ES can be either uniform when $\Delta r = const, z_1 = z_k = const$, or non-uniform $\Delta r = const, z_1 \neq z_k$ (Fig. 3).

In contrast to the planar structure of the ES, the number of parameters of the synthesis problem increases, i.e. the height of the coils above TO z_0 is added $J=f(x, y, r, z_0)$. As in the simpler case of the planar design of the probe, one cannot do without the ECP metamodel $\hat{J}=f(x, y, r, z_0)$, which significantly reduces the calculation time and it becomes possible to solve the synthesis problem.

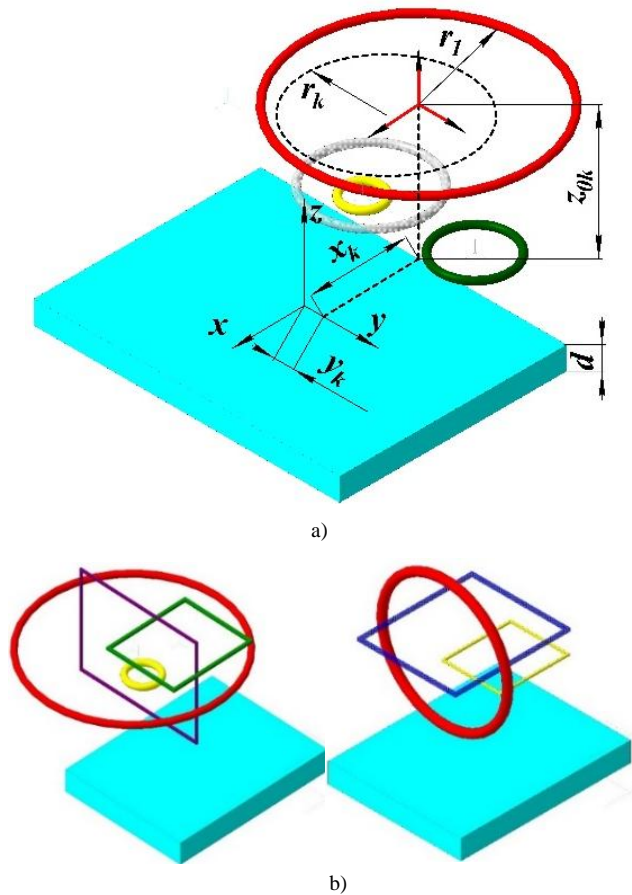


Fig. 2 Volumetric structures of ES ECP: a) homogeneous; b) heterogeneous

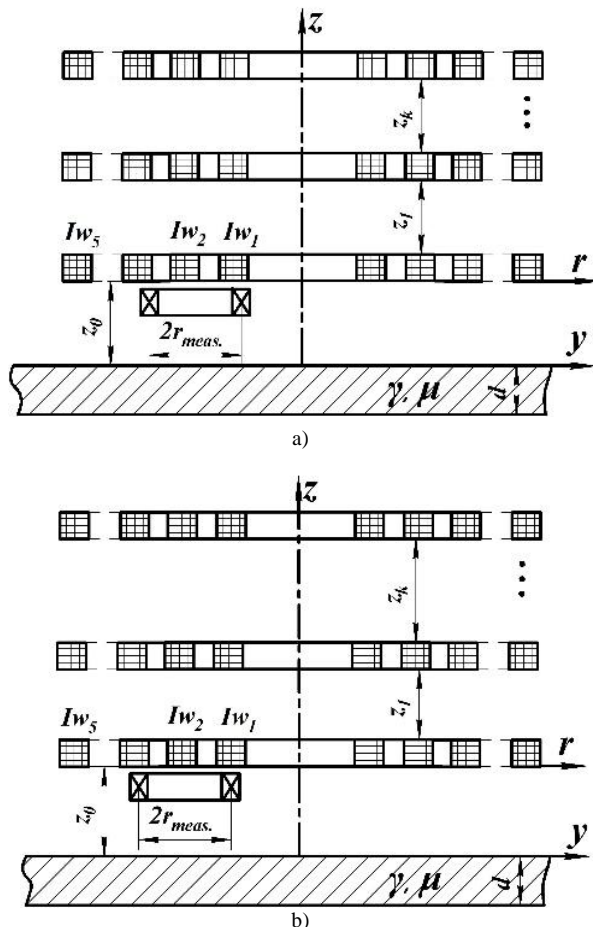


Fig. 3 Arrangement of sections of coils of surface ECP's of a volumetric homogeneous structure ES: a) uniform $\Delta r = \text{const}$, $z_1 = z_k = \text{const}$; b) non-uniform $\Delta r = \text{const}$, $z_1 \neq z_k$

The aim of the work is constructing a multiparameter hybrid RBF-metamodel of eddy current probes with volumetric homogeneous excitation structure.

On the basis of a mathematical model of a moving surface ECP, which was obtained analytically by solving the direct problem of electrodynamics in the form of Maxwell's differential equations [6], a neural network metamodel that takes into account the change in four parameters simultaneously $\hat{J}=f(x, y, r, z_0)$ was constructed.

The metamodel for the moving structure of the ES ECP in the form of ampere-coils located at different heights above the TO (Fig. 3) with the following initial data: TO thickness $d = 10$ mm; excitation current frequency $f = 5$ kHz; electrophysical parameters of the material TO $\sigma = 3,745 \cdot 10^7$ Sm/m, $\mu_r = 1$, the speed of the probe relative to TO $\vec{v} = (40, 0, 0)$ m/s was constructed. Variable model parameters are: spatial coordinates of the testing zone $x = -45 \dots 45$ mm; $y = 0 \dots 35$ mm; the radii of the coils ES $r = 2 \dots 15$ mm; their height above TO $z_0 = 2 \dots 5$ mm.

Next, the construction of a metamodel of a moving surface ECP in accordance with the algorithm proposed in [6, 7] is performed. It is advisable to approximate the multidimensional response surface using the heuristic method based on artificial neural networks. This method has some significant advantages in comparison with well-known methods [9]. An RBF-neural network with a Gaussian activation function as a multidimensional approximator was used. However, unlike the simpler case of an optimization problem with three variables, a number of difficulties arise in this case. Firstly, the response surface has a complex topography, which imposes certain limitations associated with the need to use a big data array in the procedure of training a neural network. Secondly, there is a big range of ECDD values in the range of radius changes. This is especially true for the region beyond the ES, which entails an ununiform distribution of the ECDD values at the points of the experiment plan (Fig. 4), which necessitates the decomposition of the search space. All this greatly complicates the constructing of a multiparameter metamodel and it is almost impossible to implement it on the simplest, so-called single RBF-neural networks.

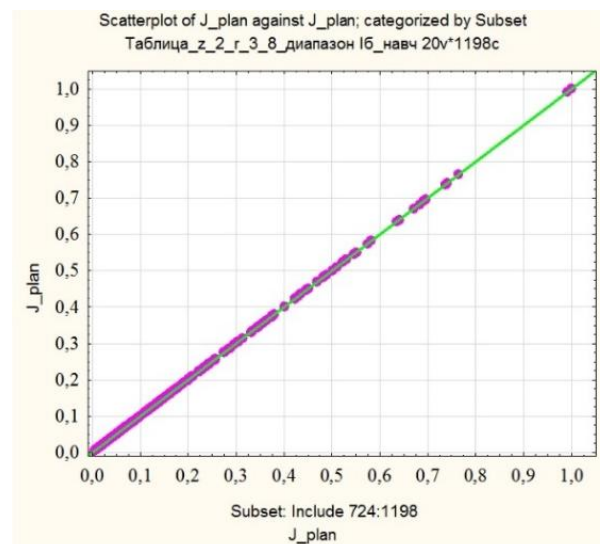


Fig. 4 Normalized ECDD values for the subregion $I_z - III_z$ of the testing zone beyond the ES

The decomposition along the height of the probe and along the radius manages to partially level a number of these difficulties. The decomposition along the height of the probe above the TO is performed into three subregions: I_z ($2 \leq z \leq 3$ mm), II_z ($3 < z \leq 4$ mm), III_z ($4 < z \leq 5$ mm). The decomposition along the radius of the coil turns is performed into six subregions: I_r ($2 \leq r \leq 3$ mm), II_r ($3 < r \leq 5$ mm), III_r ($5 < r \leq 8$ mm), IV_r ($8 < r \leq 10$ mm), V_r ($10 \leq r \leq 12$ mm), VI_r ($12 < r \leq 15$ mm). Additionally, if necessary, the radius of the search space is further divided into two subregions - directly under the turns of the coil

sections and beyond them. In order to construct the metamodel as accurately as possible, the number of points of the experiment plan at which the eddy current density is calculated is set different for the area under the turns of the coil sections and beyond them. Thus, it is possible to simplify the architecture of a single RBF-neural network and achieve a certain balance between the accuracy of the construction of the metamodel and the number of points in the experiment plan of the $N_{training}$. In this case, not classical methods of experiment planning are used, but computer methods of homogeneous filling with search points of hyperspace, namely, points of the Sobol's LP_τ -sequence $\zeta_1, \zeta_2, \dots, \zeta_{52}$ [10]. So, for example, for the subregion I_{z_0} and all subregions along the radius $I_r - VI_r$, where such LP_τ -sequences as $\zeta_1, \zeta_2, \zeta_3, \zeta_4$ in the region immediately under the coil sections, and $\zeta_1, \zeta_3, \zeta_4, \zeta_2$ realized beyond it. Those, we have the arrangement of points of the LP_τ -sequence in a multifactorial space, respectively, in the x and y coordinates of the testing zone, in the radius r of the excitation coils and the height of their location above the TO z_0 (Fig. 5). The number of points for each subregion is set individually depending on the size of the excitation coil and, accordingly, the size of the region under it. Accounting the symmetry of the ECDD concerning to the coordinate axes also influences the choice of the number of points, i.e. for a moving probe they are specified for I and II quadrants. For example, for $I_z - II_r$ the size of the testing area directly under the coil is $x = -17..17$ mm; $y = 0..13.5$ mm. For the most accurate description of the behavior of the response surface, the number of points for the training sample was chosen $N_{training} = 1749$ (Fig. 6), while beyond the region - $N_{training} = 1198$.

3D Scatterplot of r against x and y; categorized by Subset and Subset
Таблица_z_2_r_3_8_диапазон I6_навч 21v*1223c

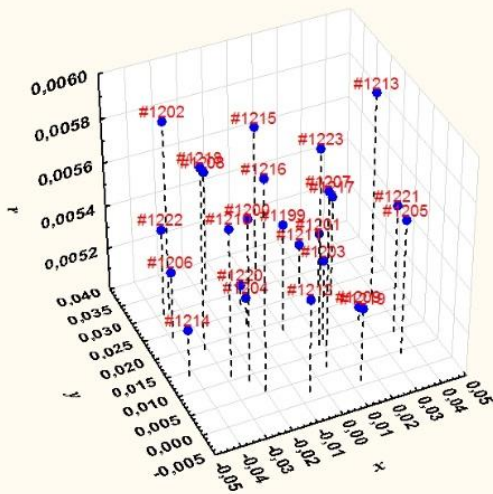


Fig. 5 Arrangement of points of the LP_τ -sequence $\zeta_1, \zeta_3, \zeta_4, \zeta_2$ in three-dimensional factor space for $r = 5..6$ mm at a fixed height $z = 2$ mm

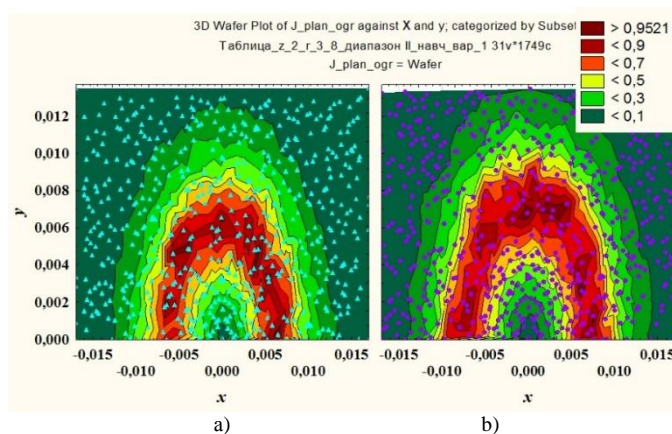


Fig. 6 A training sample, presented in the form of lines of ECDD, with points of the LP_τ -sequence for the $I_z - III_r$ subregion: a) $r = 6 - 7$ mm; b) $r = 7 - 8$ mm

Acceptable accuracy of the metamodel was obtained using hybrid neural network construction. This implies the construction of several cascades of neural networks with subsequent additional application at each committees cascade (Fig. 7) [6]. As a function of activation of neurons in a hidden layer of an RBF-network the Gauss function is used. Then the output of the neural network is formed by a linear combination of the outputs of the neurons of the hidden layer and is described by the formula:

$$\hat{J}(x, y, r, z) = \sum_{i=1}^m w_i \cdot \exp \left(- \frac{(x - c_{xi})^2 + (y - c_{yi})^2 + (r - c_{ri})^2 + (z - c_{zi})^2}{a_i^2} \right),$$

where m is the number of neurons in the hidden layer; w_i is the weighting coefficient of the output neuron with the i -th neuron of the hidden layer; $c_{xi}, c_{yi}, c_{ri}, c_{zi}$ are coordinates of the center of the i -th neuron; a_i - the width of the i -th neuron.

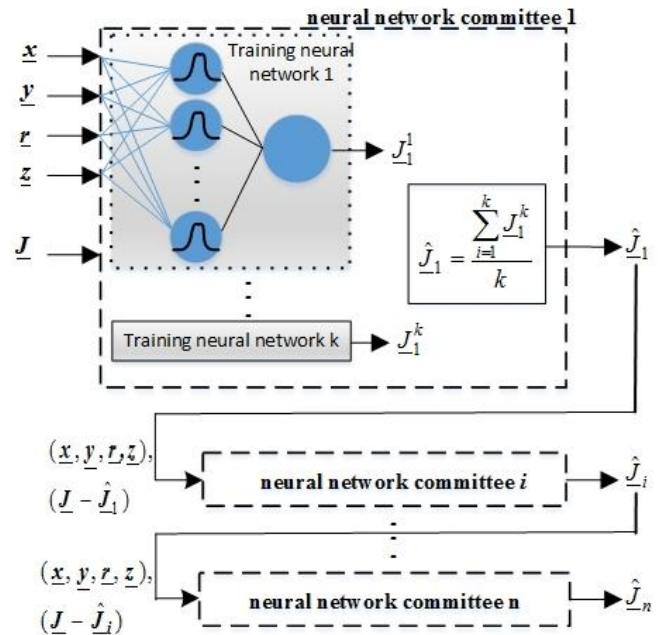


Fig. 7 Hybrid construction of a neural network metamodel

For the network's committee only networks with the productivity of the training, testing, and controlling samples of more than 90 % are used. The number of cascades is determined by the obtained value of the mean absolute percentage error MAPE, %. The best models were selected according to a combination of objective statistical indicators [10] and a subjective assessment of dispersion diagrams and histograms of residues.

Table 1 shows the obtained values of MAPE, % at the stage of training and reconstitution of neural networks for several decomposition subregions.

4. Results and discussion

Verification of the metamodel was carried out by checking the correctness of reconstitution of the response surface in all subregions on the sample, which has a bigger number of points than during training, i.e. $N_{reconstitution} > N_{training}$. To illustrate this, Fig. 8 shows the dispersion diagrams of the values of the multidimensional approximation function for one of the $I_z - III_r$ subregions at the stages of training the neural network and its reconstitution.

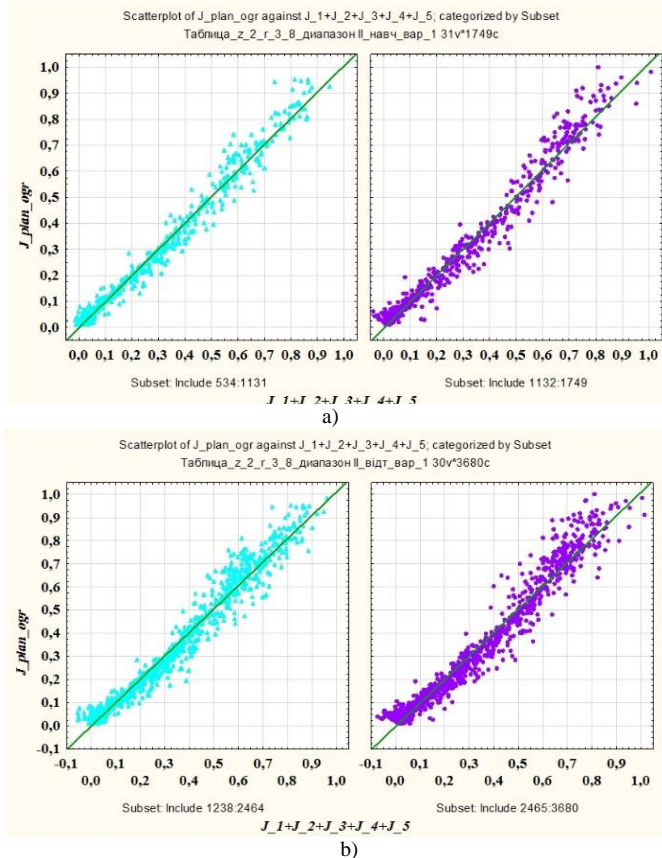


Fig. 7 Diagram of the dispersion of the values of the multi-dimensional approximation function for the subregions I_2-III_r : a) the stage of training the neural network; b) the stage of reconstitution

The adequacy of the obtained metamodel was evaluated according to the statistical F-criterion based on the following indicators: the sum squares of the regression and residues ones; the average square of the regression and residuals at a significance level of 5 % [10]. The information content of the constructed metamodel is controlled by the coefficient of determination.

Table 1: Values of MAPE,% of the obtained multi-parameter hybrid neural network metamodel of ECP for several decomposition subregions.

Decomposition subregions	$N_{training}/N_{reconstitution}$	MAPE,%	
		stage training	stage reconstitution
I_2-III_r (beyond coil)	1198/2186	16,72	21,17
I_2-III_r (under coil)	1749/3680	19,09	21,31
II_2-I_r (under coil)	900/1250	4,35	6,22

Thus, due to the use of hybrid construction of multiple neural networks using decomposition of the search space, an acceptable error in the metamodel of the volumetric structure of the ES EDP is obtained.

5. References

[1] Steblev, Yu. I. Synthesis of eddy current probes with a given structure of the excitation field in the testing zone. Defectoscopy, 1986, issue 4, pp. 58-64.

[2] Halchenko, V. Ya., Pavlov, O. K., Vorobyov, M. O. Nonlinear synthesis of magnetic fields of excitation of eddy-current probes of flaw detectors. Methods and instruments of quality testing, 2002, issue 8, pp. 3-5.

[3] Gal'chenko, V. Ya., Vorob'ev, M. A. Structural synthesis of attachable eddy-current probes with a given distribution of the probing field in the test zone. Russian Journal of Nondestructive Testing, 2005, vol. 41, issue 1, pp. 29-33. doi:10.1007/s11181-005-0124-7.

[4] Halchenko, V. Ya., Trembovetska, R. V., Tychkov, V. V. Linear synthesis of non-axial surface eddy current probes. International Journal "NDT Days", 2019, vol. 2, issue. 3, pp. 259-268.

[5] Trembovetska, R. V., Halchenko, V. Ya., Tychkov, V. V. Optimal surrogate parametric synthesis of surface circular non-axial eddy-current probes with uniform sensitivity in the testing zone. Visnyk of Kherson National Technical University, 2019, vol. 69, part 2, issue 2, pp. 118-125.

[6] Halchenko, V. Ya., Trembovetska, R. V., Tychkov, V. V., Storchak A. V. Nonlinear surrogate synthesis of the surface circular eddy current probes. Przegląd elektrotechniczny, 2019, vol. 95, issue 9, pp. 76-82. doi:10.15199/48.2019.09.15

[7] Halchenko, V. Ya., Trembovetska, R. V., Tychkov, V. V. Development of excitation structure RBF-metamodels of moving concentric eddy current probe. Electrical engineering & electromechanics, 2019, issue 2, pp. 28-38. doi: 10.20998/2074-272X.2019.2.05.

[8] Trembovetska, R. V., Halchenko, V. Ya., Tychkov, V. V., Storchak A. V. Estimation of accuracy of neuro-network metamodels of surface eddy current probes. Visnyk Cherkassy State Technological University. Seriya: Tehnichni nauky, 2019, issue 2, pp.18-29. doi:10.24025/2306-4412.2.2019.171272

[9] Haykin Simon. Neural Networks: A Complete Course. Moscow, Williams Publ. House, 2006. 1104 p.

[10] Halchenko, V. Ya., Trembovetska, R. V., Tychkov, V. V. The neurocomputing using of the development metamodels stage in the optimal surrogate antennas synthesis process. Visnyk NTUU KPI. Seriya - Radiotekhnika Radioaparotobuduvannia, 2018, vol. 74, pp. 60-72. doi:10.20535/RADAP.2018.74.60-72.

MODELING THE NUMBER OF ERRORS THAT THE CODE SURELY DETECTS

Prof. Ilievska N. PhD.

Faculty of Computer Science and Engineering, "Ss. Cyril and Methodius" University, Skopje, R. N. Macedonia
 natasa.ilievska@finki.ukim.mk

Abstract: The codes for error control (error-detecting and error-correcting codes) are extremely important part of the communication systems and storage devices, ensuring reliable data transmission and storage. In this paper using simulations, we analyze an error-detecting code. More specifically, we will be focused on the error-detecting capability of the code. Namely, using simulations we will obtain the number of errors that the code detects for sure, as an important parameter of every error-detecting code.

Keywords: ERROR-DETECTING CODE, CODED BLOCK, SYMBOL, ALPHABET

1. Introduction

When data is transmitted through or stored on some medium, due to the noises in the medium or other external influences, there is a possibility of errors. This means that the data received by the recipient may not be identical to those sent through the communication channel or data recorded on the storage. Therefore, there is a need to check that the data is correct. Checking is done using the codes for error control. There are two basic types of these codes: error-correcting and error-detecting codes. While the first ones have ability to correct up to some number of incorrectly transmitted bits, there are slower in their work. The error-detecting codes are faster and are in advantage in networks where errors rarely occur. There are various error-detecting codes: from very simple as parity bit ([1]) and repetition code ([2]) to more complex as checksum ([3], [4]), CRC ([5], [6]), etc. In our previous work we have also defined some error-detecting codes ([7], [8], [9]).

All error-detecting codes add redundant symbols on the input blocks, which are later used by the receiver in order to check whether there are errors in transmission. If the code detects that some data is incorrectly transmitted, it asks for retransmission of that data [10].

For every error-detecting code it is possible that there will be errors in transmission that the code will not detect. Therefore, before any code is implemented, it is important to know the ability of the code to detect errors. In this regard, it is important to know up to which number of incorrectly transmitted bits, the code will detect the error for sure. In this paper we will analyze an error-detecting code in the light of this parameter - the number of errors that the code surely detects. The number of errors that the code surely detects is the maximum number of incorrectly transmitted bits up to which the code will surely detect the error in transmission.

2. Definition of the Error-Detecting Code

Let A and B be non-singular binary matrices of order $s \times s$, and let C be a binary matrix of order $1 \times s$. The alphabet is $\Sigma = \{0, 1, \dots, 2^s - 1\}$. We choose the parameter r of the model, which should be a non-negative integer.

Let the input block be $a_0 a_1 \dots a_{n-1}$, where all symbols a_i are from the alphabet Σ . Then the redundant symbols are defined using the following equation:

$$(1) \mathbf{d}_i = \mathbf{a}_i A^{n-2} + \sum_{j=1}^{n-2} \mathbf{a}_{i+j} B A^{n-j-2} + C \sum_{j=0}^{n-3} A^j, \quad i=0, 1, \dots, r$$

where n is the length of the input block, r is the model's parameter that is an integer which satisfies the condition $1 \leq r \leq n-1$. Bolded symbols are the binary representations of the corresponding symbols as $1 \times r$ vectors, i.e., \mathbf{a}_i is the binary representation of the information symbol a_i , $i=0, 1, \dots, n-1$, while \mathbf{d}_i is the binary representation of the redundant symbol d_i , $i=0, 1, \dots, r$. A , B and C are the binary matrices that are used for coding. The operation $+$ is binary addition and all operations in indexes are modulo n .

After calculating the redundant symbols, the binary form of the input block $\mathbf{a}_0 \mathbf{a}_1 \dots \mathbf{a}_{n-1}$ is extended into a block $\mathbf{a}_0 \mathbf{a}_1 \dots \mathbf{a}_{n-1} \mathbf{d}_0 \mathbf{d}_1 \dots \mathbf{d}_r$.

With this is obtained the binary form of the coded block, which is transmitted through the binary symmetric channel.

From the above definition of the model we can see that this code always adds $r+1$ redundant symbol on each input block, regardless of its length. As we can see from the constrains for the parameter of the code r , the length of redundancy must not exceed the length of the input block.

When the receiver receives the output block, in order to ensure that it has a correct block, it calculates the redundant symbols using equation (1). If the calculated symbols are identical with the received ones, it accepts the block as correctly transmitted. In opposite, the receiver concludes that the block is not correctly transmitted. In that situation, the receiver asks the sender to send the block once again. But, there is always a small chance to have errors in transmission and at a same time the calculated by the receiver symbols to be equal to the received redundant symbols. This means that it is possible to have undetected errors in transmission. Therefore, it is important to know up to which number of incorrectly transmitted bits, the code will surely detect the error, which is exactly the subject of this paper.

But, first let see the coding procedure in the following example.

Example: In this example we will demonstrate the coding procedure. Let the following binary matrices of order 3×3 are used for coding:

$$A = \begin{bmatrix} 1 & 0 & 1 \\ 0 & 1 & 1 \\ 1 & 1 & 1 \end{bmatrix}, B = \begin{bmatrix} 0 & 1 & 1 \\ 1 & 1 & 1 \\ 1 & 0 & 1 \end{bmatrix}, C = [0 \ 0 \ 0]$$

The alphabet is $\Sigma = \{0, 1, 2, 3, 4, 5, 6, 7\}$.

Let suppose that the parameter of the model is $r=2$ and input block $a_0 a_1 a_2 a_3 a_4 = 46320$ of length $n=5$ symbols from the alphabet is coded. Then, the binary representations of the information symbols are $\mathbf{a}_0 = [1 \ 0 \ 0]$, $\mathbf{a}_1 = [1 \ 1 \ 0]$, $\mathbf{a}_2 = [0 \ 1 \ 1]$, $\mathbf{a}_3 = [0 \ 1 \ 0]$ and $\mathbf{a}_4 = [0 \ 0 \ 0]$. The redundant symbols are calculated using (1), i.e.:

$$\mathbf{d}_i = \mathbf{a}_i A^3 + \mathbf{a}_{i+1} B A^2 + \mathbf{a}_{i+2} B A + \mathbf{a}_{i+3} B, \quad i=0, 1, 2.$$

First, we obtain the matrices:

$$A^3 = \begin{bmatrix} 0 & 1 & 1 \\ 1 & 0 & 1 \\ 1 & 1 & 1 \end{bmatrix}, B A^2 = \begin{bmatrix} 1 & 0 & 1 \\ 1 & 1 & 1 \\ 0 & 1 & 1 \end{bmatrix}, B A = \begin{bmatrix} 1 & 0 & 0 \\ 0 & 0 & 1 \\ 0 & 1 & 0 \end{bmatrix}$$

Now,

$$\mathbf{d}_0 = \mathbf{a}_0 A^3 + \mathbf{a}_1 B A^2 + \mathbf{a}_2 B A + \mathbf{a}_3 B = [1 \ 0 \ 0] \begin{bmatrix} 0 & 1 & 1 \\ 1 & 0 & 1 \\ 1 & 1 & 1 \end{bmatrix} +$$

$$[1 \ 1 \ 0] \begin{bmatrix} 1 & 0 & 1 \\ 1 & 1 & 1 \\ 0 & 1 & 1 \end{bmatrix} + [0 \ 1 \ 1] \begin{bmatrix} 1 & 0 & 0 \\ 0 & 0 & 1 \\ 0 & 1 & 0 \end{bmatrix} + [0 \ 1 \ 0] \begin{bmatrix} 0 & 1 & 1 \\ 1 & 1 & 1 \\ 1 & 0 & 1 \end{bmatrix} =$$

$$=[1 \ 0 \ 1]$$

$$\mathbf{d}_1 = \mathbf{a}_1 A^3 + \mathbf{a}_2 B A^2 + \mathbf{a}_3 B A + \mathbf{a}_4 B = [1 \ 1 \ 0] \begin{bmatrix} 0 & 1 & 1 \\ 1 & 0 & 1 \\ 1 & 1 & 1 \end{bmatrix} +$$

$$\begin{aligned}
 & \begin{bmatrix} 1 & 0 & 1 \\ 0 & 1 & 1 \end{bmatrix} + \begin{bmatrix} 1 & 0 & 0 \\ 0 & 0 & 1 \\ 0 & 1 & 0 \end{bmatrix} + \begin{bmatrix} 0 & 1 & 1 \\ 1 & 1 & 1 \\ 1 & 0 & 1 \end{bmatrix} = \\
 & = \begin{bmatrix} 0 & 1 & 1 \\ 1 & 0 & 1 \\ 1 & 1 & 1 \end{bmatrix} \\
 & d_2 = a_2A^3 + a_3BA^2 + a_4BA + a_0B = \begin{bmatrix} 0 & 1 & 1 \\ 1 & 0 & 1 \\ 1 & 1 & 1 \end{bmatrix} + \\
 & \begin{bmatrix} 1 & 0 & 1 \\ 0 & 1 & 1 \\ 0 & 1 & 1 \end{bmatrix} + \begin{bmatrix} 1 & 0 & 0 \\ 0 & 0 & 1 \\ 0 & 1 & 0 \end{bmatrix} + \begin{bmatrix} 0 & 1 & 1 \\ 1 & 1 & 1 \\ 1 & 0 & 1 \end{bmatrix} = \\
 & = \begin{bmatrix} 1 & 1 & 0 \\ 1 & 1 & 0 \\ 1 & 1 & 0 \end{bmatrix}
 \end{aligned}$$

The redundant symbol d_0 over the alphabet Σ is $d_0=5$, the symbol d_1 over the alphabet Σ is $d_1=3$ and the symbol d_2 is $d_2=6$. With this we obtained the coded block $a_0a_1a_2a_3a_4d_0d_1d_2=46320536$, while the binary form is $a_0a_1a_2a_3a_4d_0d_1d_2=100110011010000101011110$. This coded block in binary form is transmitted through the binary symmetric channel.

Let suppose that the 14th information bit is incorrectly transmitted. This means that if we denote the output block that receiver receives with $a_0'a_1'a_2'a_3'a_4'd_0'd_1'd_2'$, then $a_0'=a_0, a_1'=a_1, a_2'=a_2, a_3'=a_3, a_4'=[0 \ 1 \ 0] \neq a_4, d_0'=d_0, d_1'=d_1, d_2'=d_2$. The receiver checks whether the block is correctly transmitted, i.e., using (1) it calculates the redundant symbols for the received block $a_0'a_1'a_2'a_3'a_4'$.

$$d_0' = a_0'A^3 + a_1'BA^2 + a_2'BA + a_3'B = [1 \ 0 \ 1]$$

$$d_1' = a_1'A^3 + a_2'BA^2 + a_3'BA + a_4'B = [1 \ 0 \ 0]$$

$$d_2' = a_2'A^3 + a_3'BA^2 + a_4'BA + a_0'B = [1 \ 1 \ 1]$$

Since $d_1 \neq d_1'$ (also $d_2 \neq d_2'$), the receiver concludes that there are errors in transmission, i.e., the received block is not identical with the block sent by the sender. Therefore, it demands retransmission of the block.

3. Results from the Simulation Procedure

In this paper, using simulations we will obtain the number of errors that the code surely detects. In the simulation process for a given n and r , we transmit through a simulated binary symmetric channel a large number of coded input blocks of length n over the alphabet Σ . For each i from 1 to the length of the coded input blocks in binary form, we calculate the percentage of transmitted coded blocks with i incorrectly transmitted bits in which the error in transmission is not detected. The number of errors that the code detects for sure is the largest integer v such that the percentage of incorrectly transmitted coded blocks with i incorrectly transmitted bits in which the error is not detected is equal to 0% for all i from 1 to v . In order to obtain reliable and accurate results, we chose the probability of bit-error in the simulated binary-symmetric channel such that the number of incorrectly transmitted coded blocks with i incorrectly transmitted bits to be large number for small values of i , i.e., values of i smaller than or equal to v .

In the coding procedure, we use the following binary matrices A, B and C :

$$A = \begin{bmatrix} 1 & 0 & 1 \\ 0 & 1 & 1 \\ 1 & 1 & 1 \end{bmatrix}, B = \begin{bmatrix} 0 & 1 & 1 \\ 1 & 1 & 1 \\ 1 & 0 & 1 \end{bmatrix}, C = [0 \ 0 \ 0]$$

The alphabet is $\Sigma = \{0, 1, 2, 3, 4, 5, 6, 7\}$. We will consider the cases when the parameter of the model $r=2, r=3$ and $r=4$.

Since the length of the redundancy is $r+1$ symbol, follows that in the case when $r=2$, the length of the redundancy is 3 symbols from the alphabet Σ . Since the length of the input block must be greater than or equal to the length of the redundancy, in this case the length of the input block n must be greater than or equal to 3 symbols from the alphabet Σ (Fig. 1). Each element from the alphabet of order 8 is presented with 3 bits in the binary

representation. Therefore, in this case the redundancy has length 9 bits.

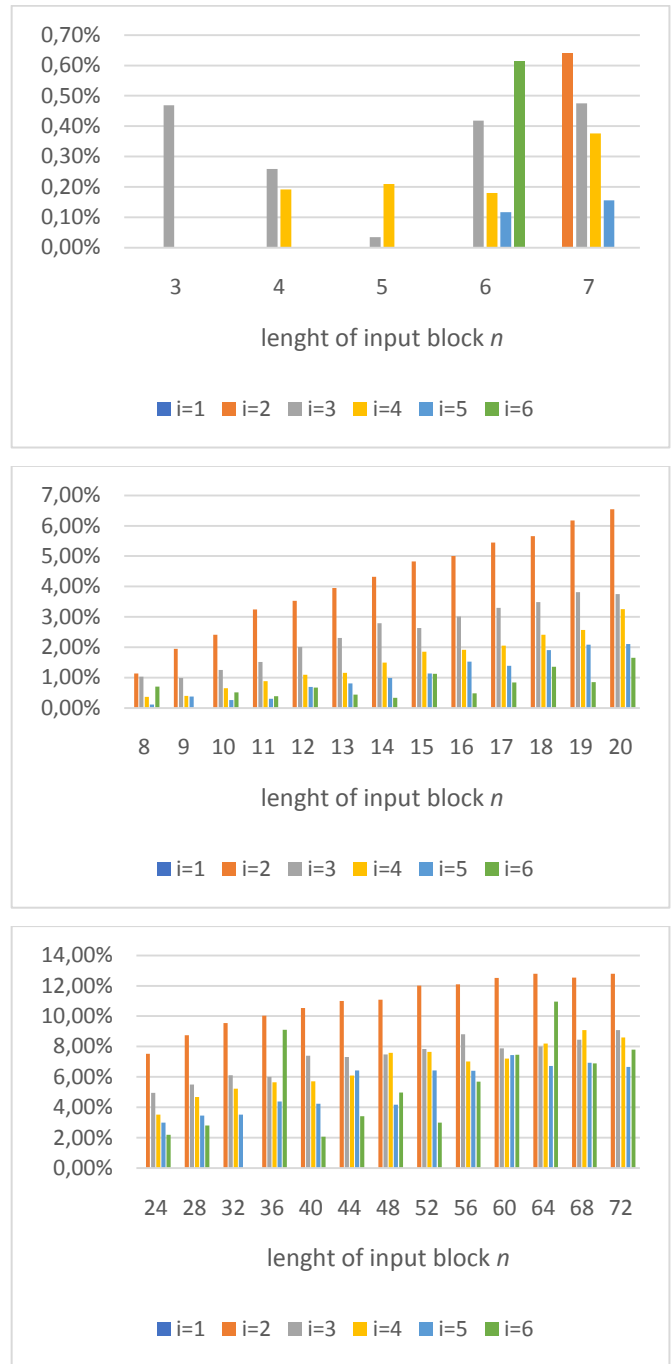


Fig. 1 Percentage of undetected incorrectly transmitted coded blocks with i incorrectly transmitted bits when input blocks have length n symbols from the alphabet Σ in the case when the redundancy is 9 bits.

In Fig. 1 are given the percentages of incorrectly transmitted coded blocks in the simulation process in which $i \leq 6$ bits are incorrectly transmitted and the error in transmission is not detected in the case when the redundancy is 9 bits ($r=2$). The length of the input blocks n is expressed in a number of symbols from the alphabet Σ . Please note that the scaling of the y-axis is different on the three graphs. For small values of the length of the input block n , the percentages of undetected incorrectly transmitted blocks with i incorrectly transmitted bits are very small. In order the results to be visible they are separated in the first figure from Fig. 1. Since the percentages of undetected incorrectly transmitted blocks with i incorrectly transmitted bits increase when n increases, the scaling of the second and third image from Fig. 1 is adjusted accordingly.

As we can see from Fig. 1, when the length of the input blocks is $n=3$ symbols from Σ , the percentage of undetected incorrectly

transmitted blocks with i incorrectly transmitted bit is different than 0% only for $i=3$. Since the code detected all incorrectly transmitted blocks with 1 or 2 incorrectly transmitted bits, but there are blocks with 3 incorrectly transmitted bits in which the error is not detected, the number of errors that the code surely detects when the length of the input blocks is $n=3$ symbols from Σ is 2. Also, in the case when the length of the input blocks is $n=4$, the smallest value of i for which the percentage of undetected incorrectly transmitted blocks with i incorrectly transmitted bits is different than 0% is 3. Therefore, we conclude that in this case the code surely detects also up to 2 incorrectly transmitted bits. The same conclusion holds also in the cases when the length of the input block n is 5 or 6 symbols from the alphabet Σ . For input blocks with length greater than or equal to 7 symbols, the percentage of undetected incorrectly transmitted blocks with 2 incorrectly transmitted bits is positive (there is the orange pillar), from where follows that in this case the code surely detects 1 incorrectly transmitted bit.

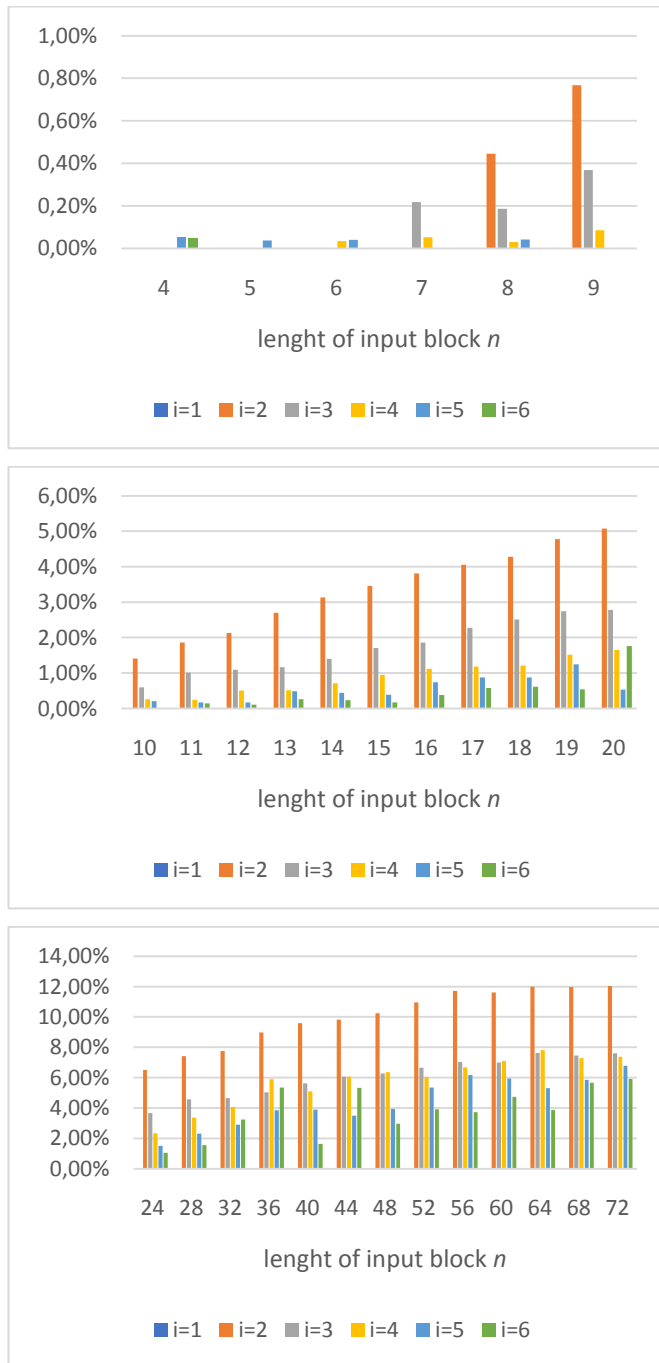


Fig. 2 Percentage of undetected incorrectly transmitted coded blocks with i incorrectly transmitted bits when input blocks have length n symbols from the alphabet Σ in the case when the redundancy is 12 bits.

The results when $r=3$ are given in Fig. 2. In this case the length of the redundancy is 4 symbols from the alphabet Σ (i.e., 12 bits in the binary representation). Therefore, in this case the length of the input block must be greater than or equal to 4 symbols from Σ . From Fig. 2, we can see that in the case when the redundancy is 12 bits, the code surely detects up to 4 incorrectly transmitted bits when the length of the input block is 4 or 5 symbols from Σ . When the input block has length 6 symbols, the code surely detects up to 3 incorrectly transmitted bits, while when the input block has length 7 symbols, the code surely detects up to 2 incorrectly transmitted bits. When the input block has length greater than or equal to 8 symbols, the code surely detects 1 incorrectly transmitted bit.

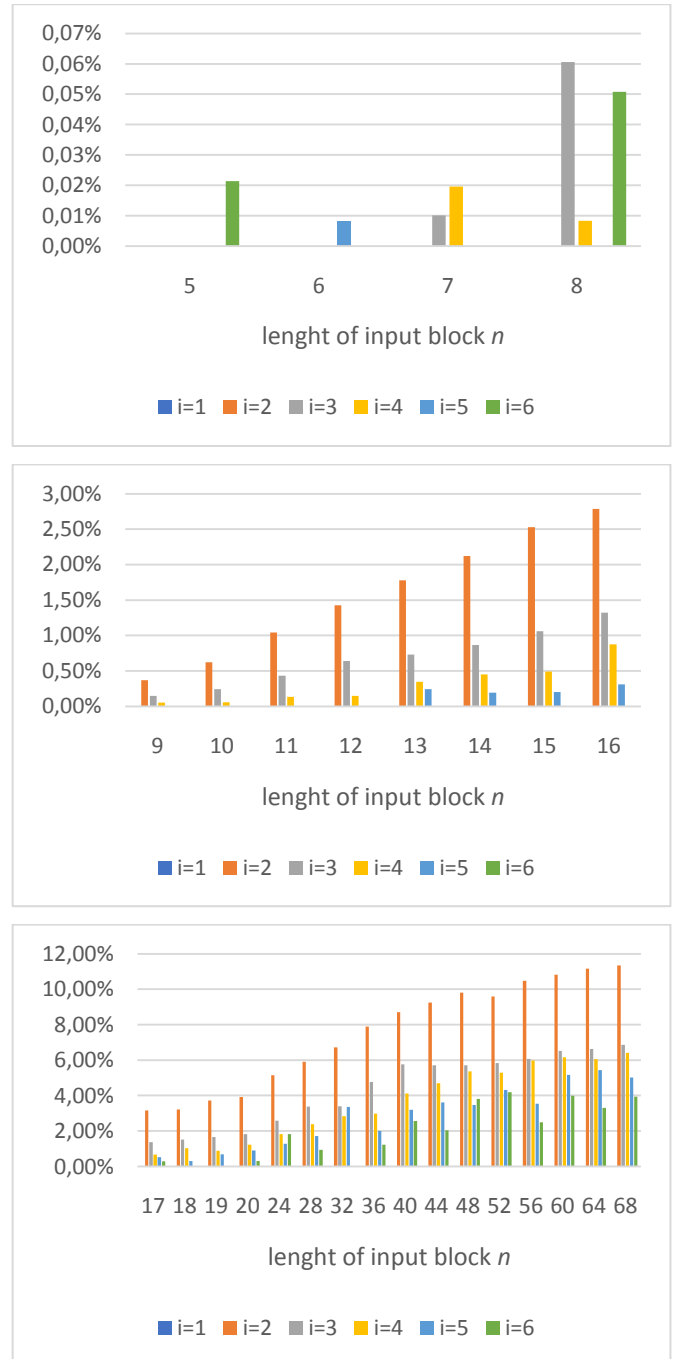


Fig. 3 Percentage of undetected incorrectly transmitted coded blocks with i incorrectly transmitted bits when input blocks have length n symbols from the alphabet Σ in the case when the redundancy is 15 bits

Similarly, when the parameter $r=4$, the redundancy is 5 symbols from Σ (i.e., 15 bits in the binary representation) and the length of the input blocks $n \geq 5$ (Fig. 3). When the length of the input block is 5 symbols, the code surely detects up to 5 incorrectly transmitted bits, while when the length of the input block is 6 symbols, the code

surely detects up to 4 incorrectly transmitted bits. For input blocks with length 7 or 8 symbols, the code surely detects up to 2 incorrectly transmitted bits. When the length of the input block is greater than 8 symbols, the code detects for sure 1 incorrectly transmitted bit.

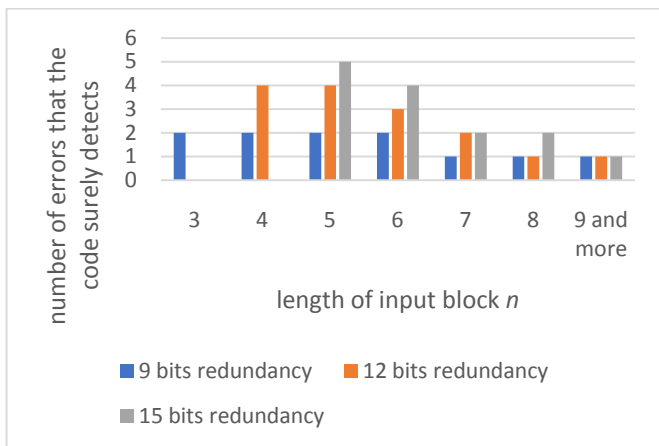


Fig. 4 Number of incorrectly transmitted bits that the code surely detects when the length of the input blocks is n symbols from the alphabet Σ and the redundancy is 9, 12 and 15 bits.

In Fig. 4 and Fig. 5 are presented the numbers of incorrectly transmitted bits that the code surely detects when the redundancy is 9, 12 and 15 bits. On x -axis in Fig. 4 is given the length of the input block, on y -axis is given the number of errors that the code surely detects, while the color of each pillar represents the length of the redundancy.

From Fig. 4 we can see that when the length of the input block is fixed, if longer redundancy is added to the input blocks, then the number of incorrectly transmitted bits that the code detected for sure is greater or at least equal to the number of surely detected incorrectly transmitted bits when a shorter redundancy is added. This is expected result since longer redundancy means that each information symbol is controlled by more redundant symbols.

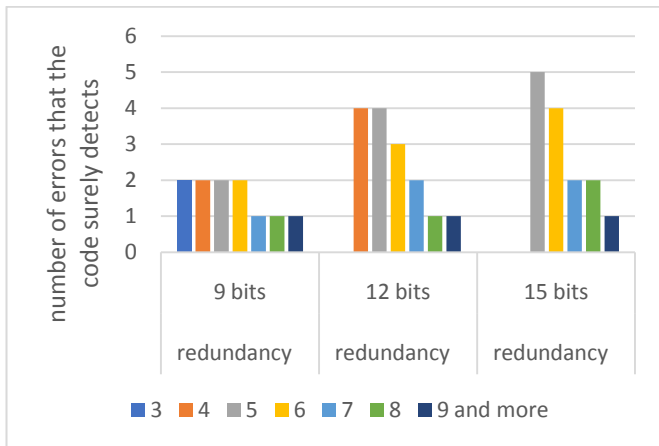


Fig. 5 Number of incorrectly transmitted bits that the code surely detects when the length of the input blocks is n symbols from the alphabet Σ and the redundancy is 9, 12 and 15 bits.

On Fig. 5 on x -axis is given the length of the redundancy, while the length of the input blocks n is represented with the color of the pillars. As we can see from Fig. 5, regardless of the length of the redundancy, when the length of the input block increases and the length of the redundancy is fixed, the number of errors that the code surely detects decreases or remains the same.

As we can see from Fig. 4 and Fig. 5, the best result from the aspect of the number of errors that the code surely detects is achieved when the length of the input blocks is 5 symbols from

the alphabet Σ and the redundancy has length 15 bits. This means that from the aspect of the number of errors that the code surely detects, it is best to divide the input message into blocks of length 5 symbols from Σ and to code these blocks such that the redundancy is 15 bits (i.e., to choose the parameter r in the model to be 4). In this case the code will detect for sure every incorrectly transmitted coded block with up to 5 incorrectly transmitted bits.

4. Conclusion

The results for the number of errors that the code surely detects when the given binary matrices A, B of order 3×3 and zero matrix C of order 1×3 are used for coding are the following:

In the case when the redundancy has length 9 bits, the code surely detects up to 2 incorrectly transmitted bits when the length of the input block is smaller than or equal to 6 symbols from Σ . For input blocks with length greater than or equal to 7 symbols, the code surely detects 1 incorrectly transmitted bit.

When the redundancy is 12 bits, the code surely detects up to 4 incorrectly transmitted bits when the length of the input block is 4 or 5 symbols from the alphabet Σ , up to 3 incorrectly transmitted bits when the input block has length 6 symbols, up to 2 incorrectly transmitted bits when the input block has length 7 symbols and 1 incorrectly transmitted bit when the input block has length greater than or equal to 8 symbols.

When the redundancy has length 15 bits, the code surely detects up to 5 incorrectly transmitted bits when the length of the input block is 5 symbols, up to 4 incorrectly transmitted bits when the length of the input block is 6 symbols, up to 2 incorrectly transmitted bits when the length of the input blocks is 7 or 8 symbols. The code surely detects 1 incorrectly transmitted bit when the length of the input block is greater than or equal to 9 symbols.

When the length of the input blocks is fixed, the number of errors the code surely detects does not decrease with increasing redundancy length. If the length of the redundancy is fixed, then when the length of the input block increases, the number of errors that the code surely detects decreases or remains the same.

In order to achieve largest number of surely detected incorrectly transmitted bits, the input message should be divided into blocks of length 5 symbols and each block to be coded separately such that the parameter of the model is $r=4$.

5. References

- [1] Ziemer R. E., Tranter W. H., "Principles of communication: systems, modulation, and noise," Wiley, 2014.
- [2] Bossert M., "Channel Coding for Telecommunications," Wiley, 1999.
- [3] Fenwick P., "Checksums and Error Control," Introduction to Computer Data Representation, Bentham Science Publishers, 2014.
- [4] Verhoeff, J., "Error Detecting Decimal Codes (Tract 29)," The Mathematical Centre, Amsterdam, 1969.
- [5] Peterson W. W., Brown D. T., "Cyclic Codes for Error Detection," Proceedings of the IRE. 49 (1), 1961, pp. 228–235.
- [6] Koopman P., "32-Bit Cyclic Redundancy Codes for Internet Applications," Proceedings of The International Conference on Dependable Systems and Networks, 2002, pp. 459–468.
- [7] Bakeva V., Ilievska N., "A probabilistic model of error-detecting codes based on quasigroups", Quasigroups and Related Systems, vol. 17, 2009, pp. 135-148.
- [8] Ilievska N., "Proving the probability of undetected errors for an error-detecting code based on quasigroups," Quasigroups and Related Systems, vol. 22, 2014, pp. 223 – 246.
- [9] Ilievska N., Gligoroski D., "Simulation of some new models of error-detecting codes," Proceedings of the 22nd Telecommunications Forum Telfor, Belgrade, Serbia, pp. 395-398, 2014.
- [10] Klove T., "Codes for Error Detection," World Scientific, 2007.

MODELING OF OVERLAP AREA OF POWDER FILTER MATERIALS

МОДЕЛИРОВАНИЕ ЗОНЫ ПЕРЕКРЫТИЯ ПОРОШКОВЫХ ФИЛЬТРУЮЩИХ МАТЕРИАЛОВ

Prof., Dr. Eng., Cor. Member of NAS of Belarus Ilyushchanka A.^{1,2},

Head of the Lab. Charniak I.², Res. Zhehdryn D.², Dr. Eng., Docent Kusin R.³,

State Research and Production Powder Metallurgy Association¹ – Minsk, Republic of Belarus

State Scientific Institution “O.V. Roman Powder Metallurgy Institute”² – Minsk, Republic of Belarus

Belarusian State Agriculture Technical University³ – Minsk, Republic of Belarus

E-mail: alexil@mail.belpak.by, irinacharniak@tut.by, 2312444@mail.ru, lerakor1974@mail.ru

Abstract: A model for calculating the permeability of two-layer powder filter materials (PFMs) is proposed taking into account the overlap area. Examples of calculating the permeability of PFMs on real powder structures are given.

KEYWORDS: TWO-LAYER POWDER FILTER MATERIALS, CALCULATION MODEL, PERMEABILITY, OVERLAP AREA.

1. Introduction

Despite the widespread use of polymeric, paper, and ceramic materials in engineering, powder filter materials compete worthy with them, especially in cases where it is necessary to realize the physico-chemical properties typical for metals and alloys from which PFMs consist. PFMs are successfully used to solve various problems: for aeration of the air flow in order to saturate the air-culture fluid with oxygen when growing aerobic microorganisms in bioreactors; for dispersion of the ozone-containing air mixture flow in order to decontaminate the fish habitat (including young fish) in recirculating aquaculture systems (RAS) and uniform distribution of vapor flow over the volume of coolant (water) to control the temperature in working tanks during heat treatment of milk, milk mixtures and technological media used in milk treatment; air, water vapor, and oil purification, as well as for other purposes [1–5].

In practice, two-layer materials are widely used to increase the operational properties of PFM. One layer is formed by fine particles and provides the necessary fineness of cleaning. The second layer is formed by coarse particles and provides sufficient strength and high permeability of PFM [6, 7]. The problem in this case is the appearance of the intermediate layer at the boundary of the layers, the so-called “overlap area”, in which smaller particles fill the pore space formed by coarse particles [8]. One of the effective ways to improve the properties of two-layer PFMs is to reduce the thickness of the fine layer [8]. In this regard, the calculation of the influence of the overlap area on the properties of two-layer PFMs is of great interest.

The purpose of this work is modeling of PFM “overlap area” and calculation of the permeability of this area.

2. Results and discussion

When two-layer materials are produced by co-molding powders of different fractions in the area of the layer boundary, smaller powder particles partially fill the pore space formed by larger particles, making, as noted above, an intermediate layer (overlap area). Figures 1 and 2 illustrate examples of the formation of such structures in the production of two-layer materials based on titanium and copper powders. We determine the effect of the overlap area on the permeability of two-layer PFMs.

To calculate the permeability taking into account the overlap area, we consider the case when the porous material consists of two layers and the overlap area. The first and second layers are respectively formed from powder particles with sizes D_1 and D_2 , with $D_1 > D_2$. The overlap area (conditionally it can be considered as the third layer), located between the first and second layers. It consists of particles of these two sizes. Small particles with sizes D_2 are located between large particles with size D_1 . We denote the thicknesses of the first layer (substrate), the intermediate layer (overlap area) and the second layer (fine powder) by h_1 , h_{12} and h_2 , and the flow rate of the filtered medium through the PFM per unit time by Q .



Fig. 1 The structure of a two-layer PFM made of titanium powders with a particle size of (minus 1000 + 400) and (minus 100 + 40) μm



Fig. 2 The structure of a two-layer PFM made of copper powders with particle sizes (minus 315 + 200) and (minus 80 + 40) μm

Considering the flow of a liquid or gas through the whole material, it is possible to write the following according to Darcy’s law [9]:

$$Q = \frac{k\Delta p}{\mu h} S, \quad (1)$$

where k – coefficient of permeability; Δp – differential pressure on PFM; S – filtration area; μ – viscosity of filtered medium; h – thickness of PFM.

For each layer separately, equation (1) can be written as follows:

$$Q_1 = \frac{k_1 \Delta p_1}{\mu h_1} S, \tag{2}$$

$$Q_{12} = \frac{k_{12} \Delta p_{12}}{\mu h_{12}} S, \tag{3}$$

$$Q_2 = \frac{k_2 \Delta p_2}{\mu h_2} S, \tag{4}$$

where $\Delta p_1, \Delta p_{12}, \Delta p_2$, - respectively, differential pressure on each of the layers with thicknesses h_1, h_{12}, h_2 ;

S – the filtration area of all layers (the first layer is the substrate; the intermediate layer is the overlap area and the second layer is fine powder).

Obviously, the flows of the filtered medium passing through the whole material Q and through each layer separately Q_1, Q_{12}, Q_2 , are equal to each other:

$$Q = Q_1 = Q_{12} = Q_2, \tag{5}$$

and differential pressure on PFM and its thickness are:

$$\Delta p = \Delta p_1 + \Delta p_{12} + \Delta p_2, \tag{6}$$

$$h = h_1 + h_{12} + h_2. \tag{7}$$

Based on (1–4), taking into account (5–7), it is possible to obtain the following equations:

$$\frac{\Delta p_1}{\Delta p} = \frac{k h_1}{k_1 h}, \tag{8}$$

$$\frac{\Delta p_{12}}{\Delta p} = \frac{k h_{12}}{k_{12} h}, \tag{9}$$

$$\frac{\Delta p_2}{\Delta p} = \frac{k h_2}{k_2 h}. \tag{10}$$

Summing up the left and right sides of equations (8–10), we obtain the equation for calculating k :

$$1 = \frac{k h_1}{k_1 h} + \frac{k h_{12}}{k_{12} h} + \frac{k h_2}{k_2 h}, \tag{11}$$

from which:

$$k = \frac{h}{\frac{h_1}{k_1} + \frac{h_{12}}{k_{12}} + \frac{h_2}{k_2}}. \tag{12}$$

To determine the coefficient of permeability in the overlap area, we have the following considerations. Surface sections blocked by large particles with sizes D_1 are excluded from the filtering process of this layer, and therefore its throughput capacity is determined by the pore space areas of the substrate filled with fine powder with an area of $S_{12} < S$. Accordingly, the coefficient of permeability of these areas can be taken equal to k_2 .

Then, on the basis of the continuity condition of the flow (5), the value of Q_{12} can be represented as:

$$Q_{12} = \frac{k_2 \Delta p_{12}}{\mu h_{12}} S_{12}. \tag{13}$$

Equating the right sides of equations (3) and (13) to each other, we obtain:

$$k_{12} = k_2 \frac{S_{12}}{S}. \tag{14}$$

To calculate S/S_{12} value, we use the elementary cell model, according to which the properties of each PFM element are determined by the elementary cell parameters in the form of a parallelepiped selected from the regular laying of 8 powder particles joined by interparticle contacts [9]. Then the value of S_{12} within such a cell varies from a minimum value equal to:

$$S_{12\min} = D_1^2 - \frac{\pi}{4} D_1^2, \tag{15}$$

to the maximum value:

$$S_{12\max} = D_1^2. \tag{16}$$

To calculate S_{12} , we take the average value of this quantity:

$$S_{12cp} = D_1^2 - \frac{\pi}{8} D_1^2. \tag{17}$$

Given that:

$$S = D_1^2, \tag{18}$$

then:

$$\frac{S}{S_{12}} = \frac{1}{1 - \frac{\pi}{8}}. \tag{19}$$

The resulted equations (11), (14) and (15) make it possible to calculate the coefficient of permeability of a two-layer PFM taking into account the overlap area between layers, knowing the values of the coefficients of permeability of the substrate and the fine layer.

Table 1 shows the results of calculations of the PFM permeability coefficients for two-layer materials, the structures of which are shown in Figures 1 and 2, and their experimental values. The values of the permeability coefficients of the substrate and the fine layer, as well as the thickness of the overlap layer are determined experimentally.

Table 1
The calculated and experimental values of the permeability coefficients of two-layer PFMs

Initial material	Powder particle size, μm		Thickness, mm			Coefficient of permeability, $\text{m}^2, \times 10^{13}$				
	Substrates	of fine layer	Substrates	of overlap area	of fine layer	Experimental values			The calculated value of two-layer PFM	
						Substrates	of fine layer	of two-layer PFM	with overlap area	without overlap area
Titanium powder	minus 1000 +400	minus 100 +40	3	1,0	1,5	180,0	7,0	14,2	11,8	23,3
Copper powder	minus 315 +200	minus 80 +40	1,7	0,3	1,0	70,0	2,16	4,17	4,19	6,1

The analysis of the data presented in the table shows, firstly, a satisfactory coincidence of the calculated and experimental data and, secondly, a significant negative effect of the overlap area on the permeability of two-layer PFMs: its presence reduces the permeability by 1.46 – 1.98 times when comparing the resulted calculations and by 1.46 – 1.64 times when comparing the results of

calculations with experimental values. This effect can be reduced by reducing the thickness of the fine layer.

Figure 3 shows the calculated dependences of the permeability coefficients of two-layer PFMs based on titanium (1) and copper (2) powders on the layer thickness of fine powder at a constant total thickness of the porous material, which, when compared with the calculated data presented in the table, indicate that, for example, a three-fold decrease in the thickness of the fine layer leads to an increase in the permeability of PFM based on titanium by 1.4 times, and based on copper – by 1.8 times. In the second case, the permeability coefficient of the material is higher than the value of the permeability coefficient of PFM with the initial thickness of the fine layer, calculated without taking into account the overlap area.

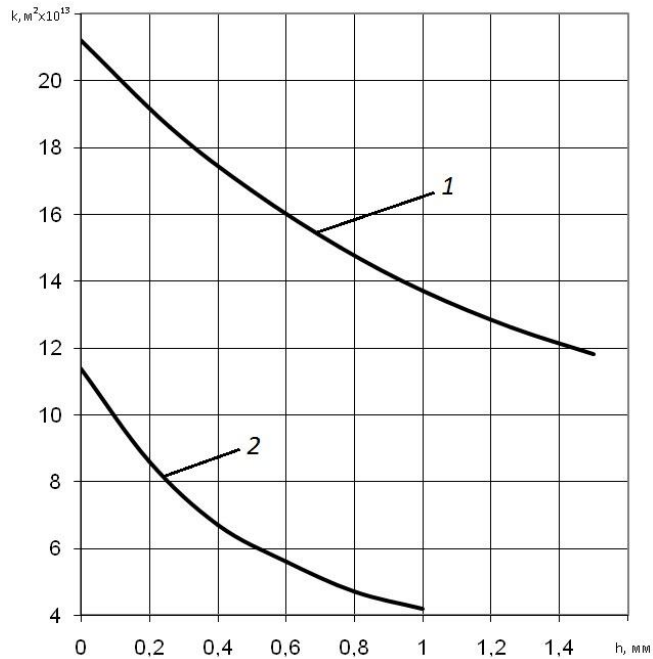


Fig. 3 The dependence of the permeability coefficient of two-layer PFM on the thickness of the fine layer:
1 – titanium-based PFM, 2 – copper-based PFM

4. Conclusion

With reference to the abovementioned, it is possible to state that the quotation obtained for calculating the permeability coefficient of two-layer PFMs with the overlap area satisfactorily agrees with experimental data. The negative effect of this area on the permeability coefficient of the porous material is shown, which, due to its presence, decreases by more than 1.46 times. It was found that this effect can be compensated by a decrease in the fine powder layer.

5. References

- [1] Ilyushchanka, A.Ph. The use of powder filter materials in the processes of cultivation of aerobic microorganisms in the processing of milk whey and heat treatment of dairy products in agro-industrial complex. – Porous permeable materials: technologies and products based on them, October 19–20, 2017, Minsk, Belaruskaya Navuka, pp. 437–442. (in Russian)
- [2] Kusin, R.A. The use of porous powder materials as gas flow distributors at enterprises of agro-industrial complex. – Current problems of the implementation of new equipment, technologies, technical service organization in the agro-industrial complex, June 7–8, 2017, Minsk, BSATU, pp. 91–96. (in Russian)
- [3] Ilyushchanka, A.Ph. The use of powder dispersants for water ozonation in recirculating aquaculture systems. – Porous permeable

materials: technologies and products based on them, Minsk, Belaruskaya Navuka, 2014, pp. 236–239. (in Russian)

- [4] Kaptsevich, V.M. Refining of industrial oils by means of powder filter materials. – Actual problems of mechanization of agricultural production, October 12–14, 2001, Gorki, BSAA, 2001, Part 2, pp. 103–108. (in Russian)
- [5] Kaptsevich, V.M. The use of porous powder material for filtering drinking water. – Actual problems of mechanization of agricultural production, October 12–14, 2001. Gorki, BSAA, 2001, Part 2, pp. 26–28. (in Russian)
- [6] Vityaz, P.A. Porous powder materials: history, current state and promising developments, 50 years old to powder metallurgy in Belarus. History, achievements, prospects, Minsk: SRP PMA, 2010, pp. 251-320. (P. Vityaz). (in Russian)
- [7] Ilyushchanka, A.Ph. Advanced materials in agricultural engineering, Minsk: BSATU, 2009, p. 256 (A. Ilyushchanka, V. Kaptsevich, R. Kusin, A. Yarkovich, A. Kusin). (in Russian)
- [8] Kusin, A.R. Improving the efficiency of two-layer powder permeable materials. – New materials, equipment and technologies in industry, Mogilev, State Institution of Higher Professional Education “Belarusian-Russian University”, 2005, p. 100). (in Russian)
- [9] Vityaz, P.A. Filter materials: properties, fields of applications, manufacturing technology, Minsk: “Research Institute of Powder Metallurgy with Pilot Production”, 1999, p.304. (P. Vityaz, V. Kaptsevich, R. Kusin). (in Russian).

MATHEMATICAL MODELING OF THE OPERATING SYSTEM OF THE CAROUSEL TYPE TRANSPLANTING MACHINE

Ass. Prof., PhD, Iurie MELNIC¹, PhD student Vladimir MELNIC²,
¹State Agrarian University of Moldova, Chisinau, Republic of Moldova
²Technical University of Moldova, Chişinău, Republic of Moldova
 iu.melnic@uasm.md, vladimir.melnic@mate.utm.md

Abstract. The main disadvantages of transplanting machine are presented in the article and the mathematical modeling of the operating system of the carousel type transplanting machine with a new method of calculation of the design parameters of the system is proposed. As a result of theoretical research of the operating system of carousel type transplanting machine the rule of motion of the point F and the mathematical model for determining initial velocity V_0 of the falling seedling have been obtained.

KEYWORDS: TRANSPLANTING MACHINE, SEEDLING, CAROUSEL TYPE, OPERATING SYSTEM, QUADRILATERAL, INITIAL VELOCITY.

Introduction

The improvement and modernization of agricultural machinery and equipment is under constant development, where increasing the working speed of machines is one of the main trends in improving their construction.

For transplanting machines, increasing the speed of work is also a very important matter in increasing the working capacity of the planting units [1, 2]. The main disadvantages of the known semiautomatic machines for planting seedlings are:

- reduced working capacity;
- low quality of planting at a higher speed of the planting unit.

In order to solve these problems, an improved construction of the carousel type transplanting machine was proposed [1]. The research of the operating system of the perfected transplanting machine is of particular importance when optimizing the main parameters of the machine. That is why determining the law of the vertical rod end movement to push the fasteners on the carousel of the transplanting machine is the basic problem of the given work.

Material and method

The drive mechanism of the carousel type transplanting machine is designed based on the quadrilateral with two arms for rotating the interminable movement mechanism, the transport of the seedlings from the coulter to the gripper, water dosing and distribution in portions.

The $OACB$ quadrilateral (fig. 1) is joined by a slider type $I-2$, which transforms the circular motion of the support wheel and drive of the planting machine into the "go-come" movement of the exit point 3. On the connecting rod 4 a sprocket for pushing the seedlings (point M) is arranged, and the vertical actuating rod (point F) of the transplanting machine carousel [3, 4] is arranged on the driven rocker 5.

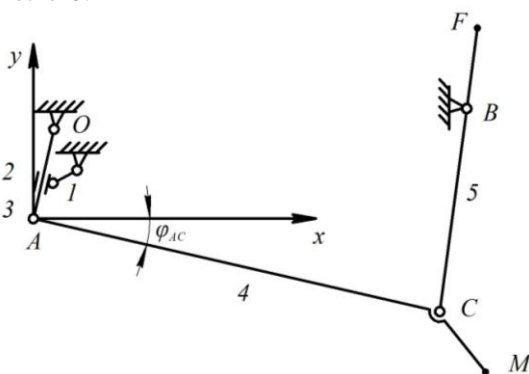


Fig.1. Kinematic diagram of the operating system of the transplanting machine:

AC - lower rod; CB - vertical rod; A - the output point of the drive mechanism; M - the end of the push pad; F - the end of the vertical rod.

Results and discussions

Let the following parameters of the drive mechanism be known: the coordinates x_0, y_0 and x_B, y_B of O and B joints, the length of the rockers $l_0=l_3$ and $l_B=l_5$, the initial φ_i and final φ_f angles of the driving rocker's return 3 with coordinates x'_M and y'_M of the point M located on the connecting rod 4 relative to the joint in point O . The coordinates $x_C(\varphi)$ and $y_C(\varphi)$ of the inner joint C , which belongs to the dyad ACB (or 3-4), are determined according to the turning angle φ of the driving rocker, through the system of equations of the circumferences with the radii l_{AC} and l_B [4, 5]:

$$x_C = \frac{(l_{AC}^2 - l_B^2 + x_B^2 - x_A^2 + y_B^2 - y_A^2) - 2y_C(y_B - y_A)}{2(x_B - x_A)}; \quad (1)$$

$$y_C = \frac{B - \sqrt{B^2 - AC}}{A}; \quad (2)$$

where: $A = F^2 + I$;

$$B = FG - Fx_A + y_A;$$

$$C = (G - x_A)^2 + y_A^2 - l_{AC}.$$

In order to determine the law of motion of the end of the vertical pushing rod (point F) it is necessary to express the ratio of the average speeds to the free and full stroke by moving the S_F of the vertical pushing rod (point F):

$$k = \frac{V_{med.cl}^F}{V_{med.cp}^F} = \frac{S_F / T_{5c.l}}{S_F / T_{5c.p}} = \frac{T_{5c.p}}{T_{5c.l}}; \quad (3)$$

where $T_{5c.p.}$ and $T_{5c.l.}$ - the period of time respectively at the full race and at the free race of the element 5, s.

If the crank angular velocity ω_j is constant:

$$\frac{T_{5c.p.}}{T_{5c.l.}} = \frac{\varphi_{1c.p.}}{\varphi_{1c.l.}}; \quad (4)$$

$$\frac{T_{5c.l.}}{T_{5c.p.}} = \frac{\varphi_{1c.l.}}{\varphi_{1c.p.}}$$

where $\varphi_{1c.p.}$ and $\varphi_{1c.l.}$ - the values of the turning angles of the crank respectively to the full and free stroke, so

$$\varphi_{1c.p.} + \varphi_{1c.l.} = 2\pi.$$

It is obvious that the periodicity of movement of the driving element 3 and the driven element 5 is equal $T_{5c.p.} = T_{3c.p.}$ and $T_{5c.l.} = T_{3c.l.}$. As a result, the coefficient of change of the average speed k is determined only by a part of the transmission mechanism, and namely, crank-slide. On the other hand, the coefficient k can be determined by the angle β between the extreme positions of the slide:

$$k = \frac{\pi + \beta}{\pi - \beta}; \quad (5)$$

The k coefficient limit is the maximum value of the acceleration a_{Mmax} of the seedling thrust pack from the coulter in

the gripper. At the uniform rotation of the crank with the angular velocity ω_1 , the acceleration a_M is equal:

$$a_M = \omega_1^2 \cdot \alpha_M, \text{ m/s}^2 \quad (6)$$

where $\alpha_M = \frac{d^2 x_M}{d\varphi_1^2}$ - the analog of the point M acceleration, which moves horizontally.

$$\alpha_M = \frac{d}{d\varphi_1^2} \left(\frac{dx_M}{d\varphi_3} \cdot \frac{d\varphi_3}{d\varphi_1} \right) = \frac{d}{d\varphi_1} (v_{M3} \cdot v_3) \quad (7)$$

where: v_{M3} - the analog of the velocity of point M compared to element 3 of the $OACB$ quadrilateral;

v_3 - the analog of the speed of the cranked part of the drive mechanism.

Taking into account that the derivative $dv_{M3}/d\varphi_3 = \alpha_{M3}$ is analogous to the acceleration of the point M with respect to element 3, and $dv_{M3}/d\varphi_1 = \varphi_3$ is analogous to the acceleration of the slider, at the result of the derivation will be obtained:

$$\alpha_M = \frac{dv_{M3} \cdot v_3 + v_{M3} \cdot dv_3}{d\varphi_1} = \frac{dv_{M3}}{d\varphi_3} \cdot \frac{d\varphi_3}{d\varphi_1} \cdot v_3 + v_{M3} \cdot \alpha_3;$$

$$\alpha_M = v_3^2 \cdot \alpha_{M3} + \alpha_3 \cdot v_{M3}.$$

Finally, the acceleration of point M becomes:

$$a_M = \omega_1^2 (v_3^2 \alpha_{M3} + \alpha_3 v_{M3}). \quad (8)$$

The kinematic characteristics of the slider as part of the driving mechanism of transplanting machine can be chosen from manuals, guidance etc [3, 4].

Then the relationship can be used to determine the velocity analog v_3 :

$$v_3 = \frac{l_1}{l_3} \cos(\varphi_1 - \varphi_3); \quad (9)$$

where: l_3 - the length of the slide;

φ_3 - the angle of return of the slide.

The variable parameters l_3 and φ_3 are determined from the relation:

$$l_3 = \sqrt{l_0^2 + l_1^2 + 2l_0 l_1 \sin \varphi_1}; \quad (10)$$

$$\varphi_3 = \arctg \frac{l_0 + l_1 \sin \varphi_1}{l_1 \cos \varphi_1}. \quad (11)$$

The analog of the slide acceleration α_3 is equal:

$$\alpha_3 = -(\alpha_{32}^k + l_1 \sin(\varphi_1 - \varphi_3)) / l_3; \quad (12)$$

where α_{32}^k - the analog of the Coriolis acceleration, which is determined by the relation:

$$\alpha_{32}^k = 2v_{32}^k v_3; \quad (13)$$

where $v_{32}^k = -l_1 \sin(\varphi_1 - \varphi_3)$ - the analog of the relative sliding speed of the slide 3 on element 2.

From this

$$\alpha_3 = 2v_3 l_1 \sin(\varphi_1 - \varphi_3) / l_3. \quad (14)$$

When passing to the next dyad 4-5, it is necessary to take into account the given length l_A of the leading rocker OA and its position dislocated relative to the slide with a constant angle $\Delta\varphi_3$:

$$\psi_3 = \varphi_3 + \Delta\varphi_3. \quad (15)$$

The formulas for determining the analogs of the angular speeds of the transmission functions v_{43} , v_{53} and the analogues of the respective angular accelerations α_{43} , α_{53} of the connecting rod 4 and of the driven rocker 5 relative to the driving one are:

$$v_{43} = -\frac{l_A \sin(\psi_3 - \varphi_5)}{l_4 \sin(\varphi_4 - \varphi_5)}; \quad (16)$$

$$v_{53} = -\frac{l_A \sin(\psi_3 - \varphi_4)}{l_5 \sin(\varphi_5 - \varphi_4)}; \quad (17)$$

$$\alpha_{43} = \frac{l_A \cos(\psi_3 - \varphi_5) - v_{53}^2 l_5 + v_{43}^2 l_4 \cos(\varphi_4 - \varphi_5)}{-l_4 \sin(\varphi_4 - \varphi_5)}; \quad (17)$$

$$\alpha_{53} = \frac{l_A \cos(\psi_3 - \varphi_4) - v_{43}^2 l_4 + v_{53}^2 l_5 \cos(\varphi_5 - \varphi_4)}{-l_5 \sin(\varphi_5 - \varphi_4)}. \quad (18)$$

The angular positions φ_4 and φ_5 in relations (17) and (18) are determined as follows:

$$\varphi_4 = \arctg \frac{y_A - y_C}{x_A - x_C}; \quad (19)$$

From the analogs of the angular characteristics of the $OACB$ quadrilateral it is easy to move to the true values of the angular velocities ω_4 and ω_5 of the angular accelerations ε_4 and ε_5 of elements 4 and 5:

$$\omega_4 = \omega_3 \cdot v_{43}; \quad \omega_5 = \omega_3 \cdot v_{53}; \quad (20)$$

$$\varepsilon_4 = \omega_3^2 \cdot \alpha_{43} + \varepsilon_3 \cdot v_{43}; \quad \varepsilon_5 = \omega_3^2 \cdot \alpha_{53} + \varepsilon_3 \cdot v_{53}. \quad (21)$$

Then the speed of point F of the vertical rod becomes equal:

$$V_F = \omega_5 l_F = \omega_3 l_F \cdot \frac{l_A \sin(\psi_3 - \varphi_4)}{l_5 \sin(\varphi_5 - \varphi_4)}; \quad (22)$$

$$V_F = \omega \cdot \frac{l_F l_A \sin(\psi_3 - \varphi_4)}{l_5 \sin(\varphi_5 - \varphi_4)}$$

Parameter V_F drives the process of dropping the seedling from the bucket into the couler by means of the initial horizontally oriented velocity V_0 . Let AB be the displacement path of the point F of the vertical rod (fig. 2).

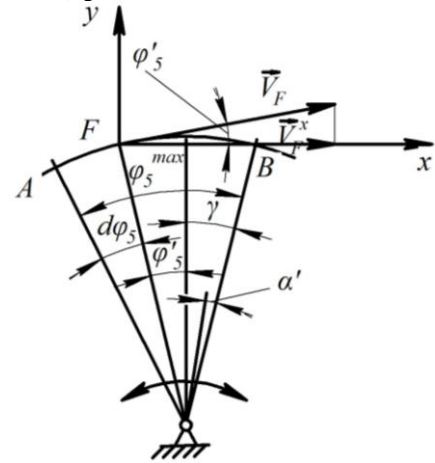


Fig.2. The displacement path of point F and the velocities diagram

Then the horizontal projection of the velocity of point F will be:

$$V_F^x = V_F \cos \varphi_5'; \quad (23)$$

where φ_5' - the angle that determines the direction of the velocity vector V_F with respect to the x -axis.

From Fig. 2 it is obvious that φ_5' is equal:

$$\varphi_5' = \varphi_5^{\max} - \gamma - d\varphi_5$$

where: γ - the displacement angle of the FC rod in the end position relative to the vertical one, rad.

$d\varphi_5$ – changes within the limits $0 \dots \varphi_5^{\max}$.

The function that describes the displacement path of point F is the following:

$$V_F^x(\varphi_5) = V_F \cos(\varphi_5^{\max} - \gamma - d\gamma_5). \quad (24)$$

Since the angular velocity of any point on the carousel (fig. 3) is equal to ω_{car} , then $\omega_f = \omega_r = \omega_{car}$, where ω_f and ω_r are respectively the angular velocities of the fastener of the interminable movement mechanism and of the seedling from the seedling cup, s^{-1} .

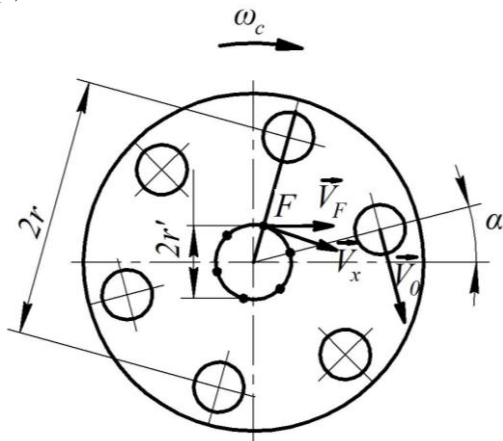


Fig.3. The diagram of the carousel during the operation of the vertical rod on the fastener

That's why the following relation is true:

$$\frac{V_f}{r'} = \frac{V_0}{r}, \quad \text{and} \quad V_0 = \frac{V_f \cdot r}{r'}; \quad (25)$$

where: V_f – fastener speed, m/s

r – radius to the center of the cups on the carousel, m

r' – radius of the fasteners arrangement, m.

Taking into account the fact that the seedling begins its fall from the cup with an advancement equal to the angle α and velocity $V_0 \neq 0$:

$$V_f(\alpha, \varphi_5) = \frac{V_F^x(\varphi_5)}{\cos\left(\frac{\pi}{n} - \alpha\right)} \quad (26)$$

where n – number of seedling cups arranged on the carousel.

The angle of the advance α of the seedlings fall from the carousel cup into the coulter can be changed in the interval $[2\pi/n; 0]$.

Substituting (24) and (26) into (25) the following function is obtained:

$$V_0(\alpha, \varphi_5) = \frac{r V_F \cos(\varphi_5^{\max} - \gamma - \varphi_5)}{r' \cos\left(\frac{\pi}{n} - \alpha\right)}; \quad (27)$$

where φ_5^{\max} – the maximum return angle of element 5 compared to its initial position, rad.

Suppose that α' is the forward angle in the vertical plan, which finds the position of point F at a forward opening of the cup equal to the angle α , then

$$d\varphi_5 = \varphi_5^{\max} - \Delta\varphi - \alpha' \quad (28)$$

where: $\Delta\varphi$ – the angle until point F contacts the fixer, rad;

$\varphi_5^{\max} - \Delta\varphi$ – the rotary phase of the carousel, rad.

In order to express α' through α , the following relation is used:

$$\varphi_5^{\max} - \Delta\varphi \dots \frac{2\pi}{n} \quad \varphi_5^{\max} - \Delta\varphi - \alpha' \dots \frac{2\pi}{n} - \alpha \quad (29)$$

From this
$$\alpha' = \frac{\alpha \cdot (\varphi_5^{\max} - \Delta\varphi) n}{2\pi}; \quad (29)$$

$$\varphi_5 = \varphi_5^{\max} - \Delta\varphi - \frac{\alpha \cdot (\varphi_5^{\max} - \Delta\varphi) n}{2\pi}. \quad (30)$$

Substituting φ_5 in (27) it is obtained:

$$V_0(\alpha) = \frac{r V_F \cos\left(\frac{\alpha n}{2\pi} \cdot (\varphi_5^{\max} - \Delta\varphi) - \gamma - \Delta\varphi\right)}{r' \cos\left(\frac{\pi}{n} - \alpha\right)}. \quad (31)$$

As according to the projected construction the forward angle is equal to α_0 , the theoretical mathematical model for determining

the initial velocity V_0 of the seedling at its movement from the seed cup into the coulter of the machine has the form:

$$V_0^{\alpha_0}(\alpha) = \frac{r \cdot V_F \cdot \cos\left(\frac{\alpha_0 \cdot n}{2\pi} \cdot (\varphi_5^{\max} - \Delta\varphi) - \gamma - \Delta\varphi\right)}{r' \cdot \cos\left(\frac{2\pi}{n} - \alpha_0\right)}. \quad (32)$$

The importance of performing the synthesis of the elaborated transplanting machine's operation system consists in the possibility of using the methodology and modeling of the operating system obtained as the result of the research.

Conclusions

1. The research of the operating system of the carousel type transplanting machine allows the determination and optimization of the essential design parameters of the improved machine.
2. There was established the law of the movement of the pushing vertical rod end of the fasteners on the carousel of the planting machine and the theoretical mathematical model for determining the initial velocity V_0 of the seedling at its movement from the seedling cup into the coulter of the machine.
3. The proposed mathematical modeling of the operating system of the carousel type transplanting machine can be used in the researching processes of the drive systems of carousel-type planters with an intermittent carousel movement.

References

1. Melnic, Iu., Bumacov, V. Mașină de plantat răsaduri. Brevet de invenție nr.2371 din 29.02.2004. - Chișinău: BOPI nr. 2/2004.
2. Мельник Ю. Повышение рабочей скорости движения рассадопосадочного агрегата. Констрування, виробництво та експлуатація сільськогосподарських машин. Zbirnic naukovih праți, випуск 39. - Кіровоград, 2009. – с. 356-362.
3. Мельник Ю. В., Бумаков В. М. Синтез заделывающего устройства рассадопосадочной машины карусельного типа. Zbirnic naukovih праți. - Kirovograd, 1997. – p.78...80.
4. Артоболевский И. И. Теория механизмов и машин: учебник для вузов. - 4-е изд., перераб. и доп. - М: Наука, 1988. - 640 с.
5. Melnic, Iu. Cercetarea sistemului de acționare a mașinii de plantat răsaduri de tip carusel. Intellectus, AGEPI, Chișinău, 2007, nr.4. – pp.75-79. ISSN 1810 7079.

RESEARCH OF MATHEMATICAL MODELS OF LITHIUM-ION STORAGEES

ИССЛЕДОВАНИЕ МАТЕМАТИЧЕСКИХ МОДЕЛЕЙ ЛИТИЙ-ИОННЫХ НАКОПИТЕЛЕЙ

PhD (Technical), Associate Professor, Plakhtii O.¹, PhD (Technical), Associate Professor, Nerubatskiy V.²,
 Postgraduate, Philipjeva M.³, Postgraduate, Mashura A.⁴
 Faculty of Mechanics and Energy^{1,2,3} – Ukrainian State University of Railway Transport, Ukraine
 Electrical Engineering Faculty⁴ – National Technical University «Kharkiv Polytechnic Institute», Ukraine
 a.plakhtiy1989@gmail.com, NVP9@i.ua

Abstract: In modern industry self-powered devices are an important component. For such devices, the most important component is the energy storage device used, most often based on lithium-ion technology. The article presents an equivalent circuits of lithium-ion batteries and a mathematical description of charge-discharge processes. Investigated in Matlab / SimPowerSystems built-in library component of lithium-ion battery. Mathematical models of equivalent circuits of different types of lithium-ionic batteries have been analyzed.

KEYWORDS: CHARGE-DISCHARGE CHARACTERISTICS, SIMULATION, LITHIUM-ION TECHNOLOGY, ENERGY STORAGE.

1. Introduction

Lithium-ion batteries are one of the most popular energy sources for a wide range of autonomous devices from mobile phones to electric vehicles [1]. At the same time mathematical models of lithium-ion batteries are one of the key issues in the modeling of autonomous devices, as they determine the capacity and time of the batteries, voltage stability during discharge, as well as the battery charge rate [2].

Nowadays, electric vehicles are attracting a lot of attention from researchers because of their properties, such as reducing fuel consumption and greenhouse gas emissions [3, 4].

As an energy storage, the battery is one of the basic elements on which the development of electric vehicles depends. The lithium-ion battery is known for its advantages such as high energy density, high charge and discharge speed, safety, etc. [5].

Until recently, a major drawback of electric vehicles was the high cost of lithium-ion batteries. However, there is a tendency to reduce the cost of lithium-ion batteries (Fig. 1). So, by the year 2030, the cost of 1 kW·h of a lithium-ion drive will cost \$ 62 [6].

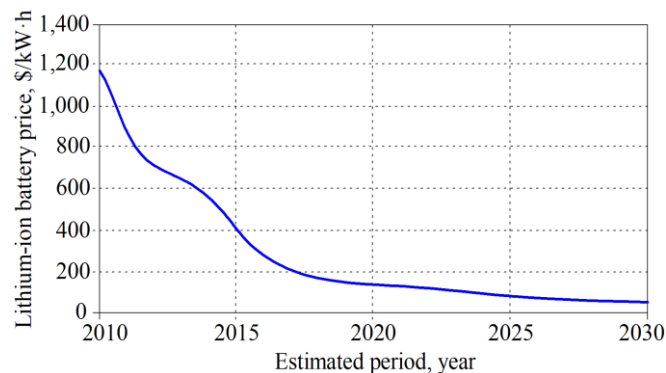


Fig. 1. The existing trend and forecast for the decrease in the cost of lithium-ion batteries

Due to the increasing research in simulation processes in lithium-ion batteries of electric vehicles, it is important to ensure a high accuracy of charge and discharge modeling [7, 8].

The purpose of this work is to analyze to validity of mathematical models of lithium-ion batteries on the example of the battery type NCR-18650b, namely, with the characteristics stated in the documentation for the battery.

2. Volt-ampere characteristics of lithium-ion batteries in the charging process

Fast charging depends on the transfer of energy to the battery at very high power levels. It is not only the chemical composition of

the battery that determines the power level at which the cell can take charge, but also the method used to charge the battery [9].

The most popular battery charging procedure is the CC–CV (Constant Current – Constant Voltage) [10] (Fig. 2).

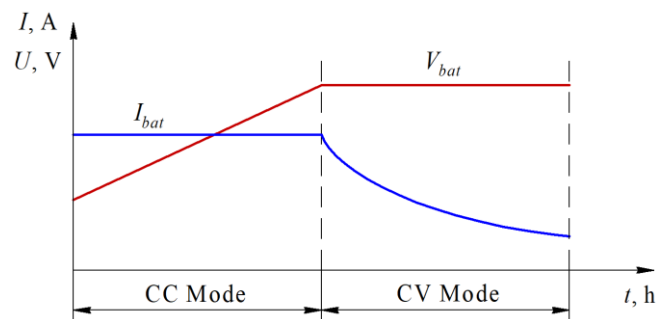


Fig. 2. The charging characteristics of the battery

The main idea behind the CC–CV method is that the battery charges a constant maximum current, usually determined by the element manufacturer, to some cut-off voltage and then charges at that voltage until current consumption decreases to about 0.1C or less, providing full charge [11, 12].

The discharge characteristics of the NCR-18650b battery according to the technical documentation are shown in Fig. 3.

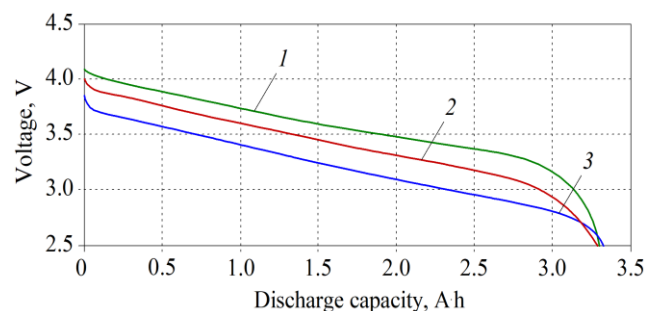


Fig. 3. The discharge characteristics of the NCR-18650b battery at load current:
 1 – 0.65 A; 2 – 3.2 A; 3 – 6.5 A

3. Equivalent circuits and mathematical models of lithium-ion storages

There are various mathematical models and equivalent circuits describing the processes in lithium-ion batteries, such as an active-resistive battery model, a dynamic resistive-capacitor model, the first and second order Thevenin model and others [13, 14]. These

models give different accuracy in the description of charge-discharge characteristics.

A model of a lithium-ion battery that takes into account the active resistance of the battery (active-resistive model of the battery) is shown in Fig. 4.

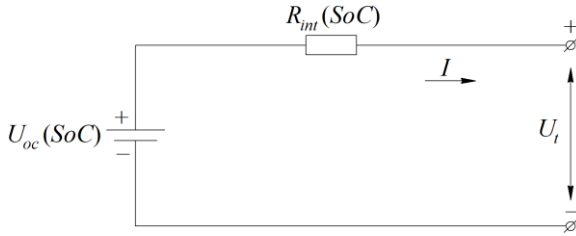


Fig. 4. Active-resistive battery model taking into account power loss

There are various options for implementing the model, in which the value of the internal resistance of the battery is either constant $R_{int} = \text{const}$, or depends on the percentage of battery charge $R_{int} = f(\text{SoC})$, where SoC is the state of charge, the percentage of battery charge. Similarly, in various models, the internal EMF of the battery can be constant $U_{oc} = \text{const}$, or it can depend on the percentage of battery charge $U_{oc} = f(\text{SoC})$.

In the case where the U_{oc} voltage and resistance depend on the percentage of charge, the output voltage at the battery terminals are expressed as [15]:

$$\begin{cases} U_t = U_{oc}(\text{SoC}) - R_{int}(\text{SoC}) \cdot I; \\ U_{oc}(\text{SoC}) = U_0 - k \cdot \text{SoC}; \\ R_{int}(\text{SoC}) = R_{int} - k_r \cdot \text{SoC}, \end{cases} \quad (1)$$

where I is the battery current; U_0 is the open circuit voltage when the battery is fully charged; k , k_r are the empirically derived coefficients.

Of the drawbacks, the model does not reduce throughput when the load increases, so it is not suitable for dynamic systems or transition states [16].

Based on the dynamic characteristics and operating principles of the battery, an equivalent circuit model was developed using resistors, capacitors as voltage sources (resistive-capacitor model) (Fig. 5).

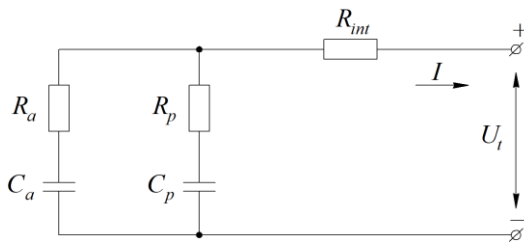


Fig. 5. Resistive-capacitor battery model

This model includes the capacitor C_a , which represents the accumulated capacitance, the series resistance R_a , which represents the polarization effect, the capacitor C_p , and the current-dependent resistance R_p , which simulates the effects of polarization and power dissipation on the internal resistance R_{int} . The C_p value is very small, while the C_a value usually takes on very large values. The SoC value is represented by the change in voltage across the capacitors C_a and C_p .

The disadvantage of this model is that the description of the discharge process has sufficiently large errors in the full discharge zone. The SoC zone of 20...80% is described quite accurately by this model.

Equations that describe battery operation:

$$\begin{cases} U_t = U_{Cp} - I_{Cp} \cdot R_p - I \cdot R_{int}; \\ U_t = U_{Ca} - I_{Ca} \cdot R_a - I \cdot R_{int}; \\ I = I_{Cp} + I_{Ca}; \\ E_C = C \cdot U^2 / 2; \\ I_C = C \cdot dU / dt. \end{cases} \quad (2)$$

The first-order Thevenin model describes charge-discharge characteristics as an active-resistive model with an additional RC circuit, which are connected in parallel. RC parameters depend on SoC , current and temperature. The first-order Thevenin model is shown in Fig. 6.

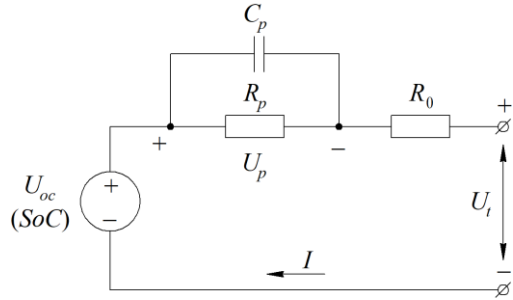


Fig. 6. Equivalent scheme of the first-order Thevenin model

The equations that describe the processes of charge-discharge of the battery are expressed as:

$$\begin{cases} U_t = U_{oc} - U_p - I \cdot R_0; \\ U_p = \frac{I}{C_p} - \frac{U_p}{C_p \cdot R_p}; \\ U_{oc} = K_0 + K_1 \cdot \ln \text{SoC} + K_2 \cdot \ln(1 - \text{SoC}), \end{cases} \quad (3)$$

where R_0 is the ohmic resistance; R_p is the polarization resistance; C_p is the polarization capacity, which is used to describe the transient during the charge-discharge of the battery.

Resistor R_0 provides the internal resistance of an element affected by SoC , temperature, and aging.

For a more accurate description of charge-discharge processes, the second-order Thevenin model is used (Fig. 7).

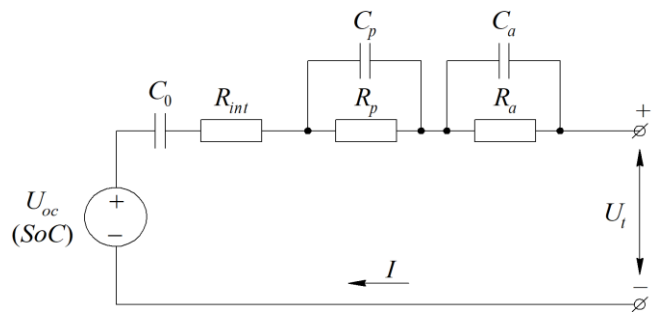


Fig. 7. Equivalent scheme of the second-order Thevenin model

The second-order Thevenin model has one additional RC component compared to the first-order model. With the optional RC component, a second-order model can achieve greater accuracy in terms of describing the transient behavior of the cell, but at the same time, the processing power increases.

The first RC circuit has a low time constant for describing short-term transient effects. These transient effects are associated with electrochemical and concentration polarization effects, including charge transfer, diffusion, and other factors.

The equations that describe the operation of the second-order Thevenin model are expressed as:

$$\begin{cases} U_t = U_{oc} - I \cdot R_{int} - U_{C1} - U_{C2}; \\ U_{C1} = -\frac{1}{C_1 \cdot R_1} \cdot U_{C1} + \frac{1}{C_1} \cdot I; \\ U_{C2} = -\frac{1}{C_2 \cdot R_2} \cdot U_{C2} + \frac{1}{C_2} \cdot I; \\ U_{oc} = K_0 + K_1 \cdot \ln SoC + K_2 \cdot \ln(1 - SoC). \end{cases} \quad (4)$$

Thus, the second-order Thevenin model is more accurate and at the same time quite simple. In accordance with the requirement for model accuracy, the number of RC components added to the model can be increased even to infinity. However, as indicated above, the complexity of the model increases with the number of RC components. A model is always selected based on a compromise between accuracy and computational complexity [17].

4. Mathematical model of lithium-ion battery in the Matlab program

In Matlab / Simulink / SimPowerSystems, there is a library component of the lithium-ion battery (Fig. 8, a). The block diagram of the battery block is shown in Fig. 8, b.

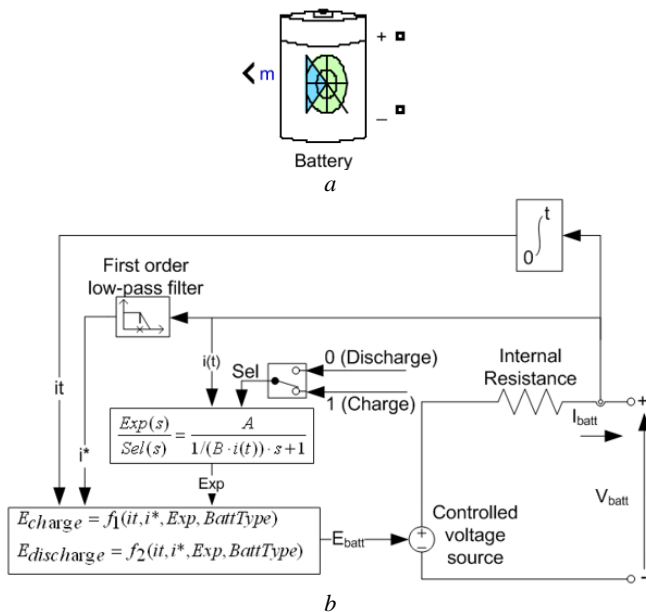


Fig. 8. Component of the lithium-ion battery: a – the appearance; b – the internal structure of the subsystem

The subsystem is the equivalent circuit of a simple linear battery model in which the internal resistance is not variable and does not depend on SoC.

In Fig. 8, b the following notation is inserted: E_{batt} is the nonlinear voltage; $Exp(s)$ is the dynamic exponential zone; $Sel(s)$ is the battery mode ($Sel(s) = 0$ during discharge, $Sel(s) = 1$ during charge).

The charge and discharge characteristics of the lithium-ion battery, which is given in Matlab, is described as expressed as:

$$f_1(it, i^*, i) = E_0 - K \cdot Q / (Q - it) \cdot i^* - K \cdot Q / (Q - it) \cdot it + A \cdot \exp(-B \cdot it); \quad (5)$$

$$f_2(it, i^*, i) = E_0 - K \cdot Q / (it + 0,1 \cdot Q) \cdot i^* - K \cdot Q / (Q - it) \cdot it + A \cdot \exp(-B \cdot it), \quad (6)$$

where it is the amount of charge consumed, A·h; i^* is the low-frequency component of the current, A; i is the battery current, A; E_0 is the constant voltage, V; K is the polarization constant, V/A·h, it is also the polarization resistance, Ohm; Q is the maximum

battery charge, A·h; A is the exponential voltage, V; B is the capacity in the exponential zone, A·h⁻¹.

5. Simulation research of lithium-ion battery in the Matlab program

The main specifications of the battery type NCR-18650b, stated in the datasheet are shown in Table 1 [10].

Table 1
The main specifications of the battery type NCR-18650b

Characteristic	Value	
Nominal capacity, A·h	3.2	
Nominal voltage, V	3.6	
Full charge time, h	4	
Weight, g	48.5	
Temperature, °C	charge	0...+45
	discharge	-20...+60
Energy density, W/kg	243	

Setting discharge parameters in the battery block in Matlab / Simulink is shown in Fig. 9.

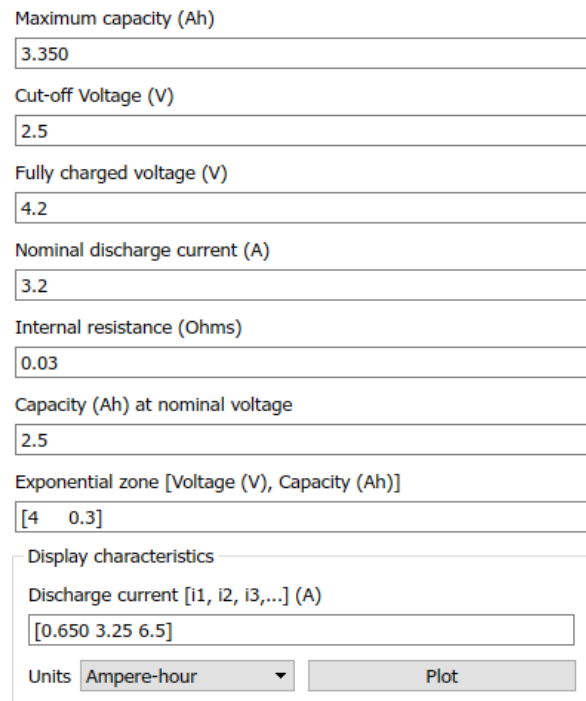


Fig. 9. Setting discharge parameters in the battery block

The characteristics of the battery discharge at different load currents obtained in Matlab / Simulink are shown in Fig. 10.

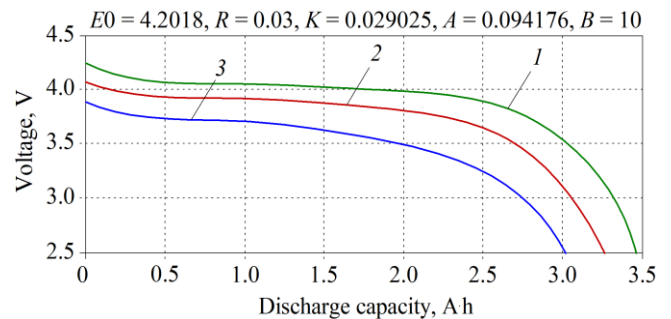


Fig. 10. Setting discharge parameters in the battery block: 1 – 0.65 A; 2 – 3.2 A; 3 – 6.5 A

Errors of the discharge characteristics of the lithium-ion battery NCR18650-b of the mathematical models considered and

the built-in Matlab model against the data presented in datasheet are shown in Table 2.

Table 2

Errors of discharge characteristics of mathematical models of lithium-ion battery NCR-18650b

Capacity testing	The relative error is given								
	At discharge current 0.65 A			At discharge current 3.2 A			At discharge current 6.5 A		
Depth of discharge range, %	0...5	5...85	85...100	0...5	5...85	85...100	0...5	5...85	85...100
Deviation of battery Matlab-model data against Datasheet	4.5	13.3	11.1	9.4	18.2	5.9	17	23	30
Active-resistive model	2.2	4.3	16.1	3.1	5.8	18.0	4.2	6.4	18.6
Resistive-capacitor model	7.7	1.7	63.6	7.1	2.1	58.1	6.8	3.2	54.2
Model Tevenin	2.1	0.8	21.4	2.0	1.1	20.1	2.0	4.3	19.7

6. Results and discussion

Analysis of the data in Table 2 showed that the most accurate is the Tevenin model in the range of 0...85 %. That is, in the range where the battery is almost completely discharged, the existing mathematical models quite accurately describe the value of the voltage on the battery. In the range of discharge 85...100 % more accurately describes the battery voltage active-resistive model.

The high error of modeling of the discharge characteristics in the built-in Matlab model of the Battery block is caused, first of all, by a non-ideal mathematical model that describes an equivalent circuit of a linear model in which the internal resistance is a constant and the value of the internal EMF depends on the magnitude of the discharge.

Therefore, to improve the accuracy of process modeling in lithium-ion batteries, it is recommended to use other substitution circuits that more accurately describe the actual behavior of the battery, such as the resistive-capacitor model, the Tevenin model, etc.

7. Conclusion

The article presents equivalent circuits of lithium-ion batteries and a mathematical description of charge-discharge processes.

In addition, the built-in library component of the lithium-ion battery was investigated.

An analysis of mathematical models of equivalent circuits of different types of lithium-ion batteries was carried out, which showed that the most accurate are the resistive-capacitor model and the Tevenin model.

8. References

- Serdnykh D. V., Tomashevsky Yu. B. Modeling of lithium-ion batteries in energy-saving complexes of autonomous objects. *Proceedings of the South Ural State University*. 2017. Vol. 17, Issue 3. P. 86–94. DOI: 10.14529/power170310.
- Franco V., Zacharopoulou T., Hammer J., Schmidt H., Mock P., Weiss M., Samaras V. Evaluation of exhaust emissions from three diesel-hybrid cars and simulation of after-treatment systems for ultralow real-world NOx emissions. *Environ. Sci. Technol.* 2019. Vol. 50, Issue 37. P. 13151–13159. DOI: 10.1021/acs.est.6b03585.
- Levay P. Z., Drossinos Y., Thiel C. The effect of fiscal incentives on market penetration of electric vehicles: a pairwise comparison of total cost of ownership. *Energy Pol.* 2017. Vol. 105. P. 524–533. DOI: 10.1016/j.enpol.2017.02.054.
- Nerubatskyi V., Plakhtii O., Ananieva O., Zinchenko O. Analysis of the Smart Grid concept for DC power supply systems. *International scientific journal «INDUSTRY 4.0»*. 2019. Vol. 4, Issue 4. P. 179–182.
- Giechaskiel B., Riccobono F., Vlachos T., Mendoza-Villafuerte P., Suarez-Bertoa R., Fontaras G., Bonnel P., Weiss M. Vehicle emission factors of solid nanoparticles in the laboratory and

on the road using Portable Emission Measurement Systems (PEMS). *Frontiers in Environmental Science*. 2015. Vol. 3. P. 82–83. DOI: 10.3389/fenvs.2015.00082.

6. Hu X., Zou C., Zhang C., Li Y. Technological developments in batteries: a survey of principal roles, types, and management needs. *IEEE Power Energy Mag.* 2017. Vol. 15. P. 20–31.

7. Safari M. Battery electric vehicles: looking behind to move forward. *Energy Pol.* 2017. Vol. 115. P. 54–65. DOI: 10.1016/j.enpol.2017.12.053.

8. Plakhtii O., Nerubatskyi V., Karpenko N., Hordiienko D., Butova O., Khoruzhevskiy H. Research into energy characteristics of single-phase active four-quadrant rectifiers with the improved hysteresis modulation. *Eastern-European Journal of Enterprise Technologies*. 2019. Vol. 5, No. 8 (101). P. 36–44. DOI: 10.15587/1729-4061.2019.179205.

9. Weiss M., Zerfass A., Helmers E. Fully electric and plug-in hybrid cars. An analysis of learning rates, user costs, and costs for mitigating CO2 and air pollutant emissions. *Clean Prod.* 2019. Vol. 212. P. 1478–1489. DOI: 10.1016/j.jclepro.2018.12.019.

10. Hardman S., Chandan A., Tal G., Turrentine T. The effectiveness of financial purchase incentives for battery electric vehicles – a review of the evidence. *Renew. Sustain. Energy Rev.* 2017. Vol. 80. P. 1100–1111. DOI: 10.1016/j.rser.2017.05.255.

11. Ciez R. E., Whitacre J. F. The cost of lithium is unlikely to upend the price of Li-ion storage systems. *Power Sources*. 2016. Vol. 320. P. 310–313. DOI: 10.1016/j.jpowsour.2016.04.073.

12. Plakhtii O., Nerubatskyi V., Sushko D., Ryshchenko I., Tsybulnyk V., Hordiienko D. Improving energy characteristics of AC electric rolling stock by using the three-level active four-quadrant rectifiers. *Eastern-European Journal of Enterprise Technologies*. 2019. Vol. 4, No. 8 (100). P. 6–14. DOI: 10.15587/1729-4061.2019.174112.

13. Plakhtii O. A., Nerubatskyi V. P., Hordiienko D. A., Tsybulnyk V. R. Analysis of the energy efficiency of a two-level voltage source inverter in the overmodulation mode. *Scientific Bulletin of National Mining University*. 2019. No. 4 (172). P. 68–72. DOI: 10.29202/nvngu/2019-4/9.

14. Xu B., Oudalov A., Ulbig A., Andersson G., Kirschen D. Modeling of lithium-ion battery degradation for cell life assessment. *IEEE Transactions on Smart Grid*. 2018. No. 9 (2). P. 1131–1140. DOI: 10.1109/tsg.2016.2578950.

15. Bryden T. S., Holland A., Hilton G., Dimitrov B., de Leon Albarran C. P., Cruden A. Lithium-ion degradation at varying discharge rates. *Energy Procedia*. 2018. Vol. 151. P. 194–198. DOI: 10.1016/j.egypro.2018.09.047.

16. Plakhtii O., Nerubatskyi V., Ryshchenko I., Zinchenko O., Tykhonravov S., Hordiienko D. Determining additional power losses in the electricity supply systems due to current's higher harmonics. *Eastern-European Journal of Enterprise Technologies*, 2019. Vol. 1, No. 8 (97). P. 6–13. DOI: 10.15587/1729-4061.2019.155672.

17. Saldana G., Martín J. I., Zamora I., Asensio F. J., Onederra O. Analysis of the current electric battery models for electric vehicle simulation. *Energies*. 2019. No. 12 (14). 27 p. DOI: 10.3390/en12142750.